Modeling SSX Spheromak Plasmas:

Internal Physics from External Measurements

Vyacheslav S. Lukin

Swarthmore College
Department of Physics & Astronomy
2000

Modeling SSX Spheromak Plasmas:
Internal Physics from External Measurements

Vyacheslav S. Lukin

Swarthmore College Department of Physics & Astronomy

500 College Avenue, Swarthmore, PA 19081

March 14, 2000

Abstract

In the recent years, computer simulations have become one of the main investigative tools in most areas of physics research. Computer modeling is also of particular importance in plasma physics, where highly dynamic nature of the conductive medium makes precise and detailed experimental measurements of the occurring processes very difficult. The Swarthmore Spheromak Experiment (SSX) studies the interaction of donut shaped magnetic structures known as spheromaks. The experimental measurements conducted on SSX can be approximately divided into two categories: 'internal' and 'external'. Internal measurements produce precise values of the quantities being measured, but cover only a small fraction of the volume of interest in the highly inhomogeneous medium and can interfere with the very processes being measured. On the other hand, external measurements are only capable of producing volume averaged values of the parameters of interest, thus integrating over the local structure and dynamics of plasma magnetofluid. We are thus forced to resort to modeling in our attempts to gain a better understanding of the physical processes taking place in the experiment. We currently employ two modeling codes: 0-D time-dependent impurity emission model, and $2\frac{1}{2}$-D resistive MHD simulation code. A VUV monochromator is used to collect time-resolved data from various plasma impurity lines. Line-ratios of the recorded intensities are then taken and compared with the predictions of the 0-D time-dependent coronal equilibrium model. Significant restrictions are thus generated on the possible values of plasma parameters such as electron temperature T_e and electron density n_e. The MHD code is employed to support our understanding of the structure and dynamics of the magnetofluid in the experiment as a whole and in the, so called, reconnection region in particular. The output of the simulation is matched with the measurements of the energetic particle's orbits and the 2-D B-field measurements.

Contents

1   Introduction

We should begin by defining what it is this thesis is about – plasma, affectionally referred to as the 4th state of matter. According to F. Chen[5], a useful definition of plasma is:

A plasma is a quasineutral gas of charged and neutral particles which exhibit collective behavior.

In this definition, the term "quasineutral" refers to the approximate local charge neutrality of plasma, so that any local concentration of positive charge produced by ionized atoms is approximately compensated by the negative charge of free electrons surrounding it in plasma. For that to be true, the density of those free electrons has to be high enough to provide a significant electrical conductivity and thus respond to and at the same time be able to generate large scale electromagnetic fields.[21] Here, we will be concerned with nearly completely ionized plasma state of hydrogen gas with very small amounts of mixed in partially ionized impurities.

Swarthmore Spheromak Experiment (SSX) is a laboratory device designed to reproduce processes happening on the solar scale, about 10^8 times the size of the experiment itself. We are particularly interested in solar flares and their interaction with each other and the surface of the sun.[4][22] Currently, the major effort on SSX is directed towards investigating the processes related to such interactions between two magnetic structures; there, reconnection of oppositely pitched magnetic structures, where the energy contained in magnetic fields is converted into thermal and kinetic energy of plasma, is of particular interest.[3][15][8]

The spheromaks produced on SSX are small size donut shaped magnetic structures (diameter less than 0.5 m) observed to reach a short lived equilibrium with lifetime of about 100 μs.[7] The magnetic fields and currents in a spheromak have helical shape that confines the plasma to a torus in such a way that a nearly force-free equilibrium is attained with the magnetic field lines parallel to the direction of the current density vector $\mathbf{J}$ (See Figure 1):

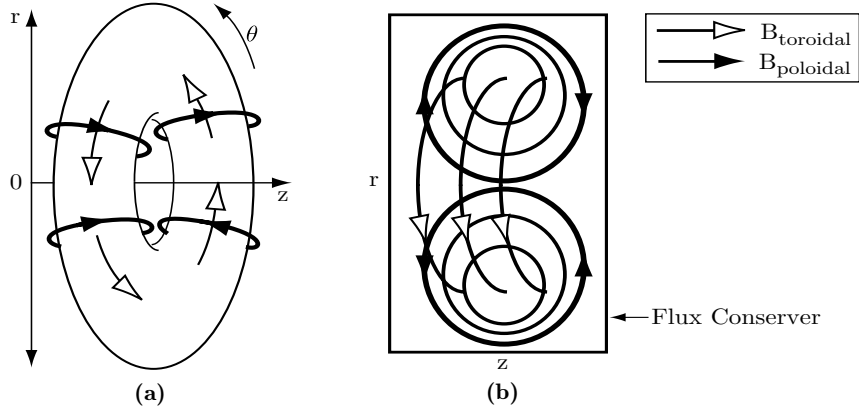$$\mathbf{J} \times \mathbf{B} \approx \mathbf{0},$$

Figure 1: Configuration of magnetic fields of a spheromak.

In SSX, spheromaks are created with a magnetized coaxial plasma gun (See Figure 2 for the spheromak formation cartoon). Small amounts of hydrogen gas introduced into the gun are first ionized and poloidal currents are induced with a 5 kV discharge. The currents in the plasma and the gun itself, in turn, generate toroidal B-fields. The interaction of the magnetic field and the currents produces the Lorentz $\mathbf{J} \times \mathbf{B}$ force, which accelerates plasma towards the opening of the gun. There, plasma confronts "stuffing B-field" produced by an external magnetic coil. As a result, according to Faraday's law, toroidal currents (poloidal magnetic field) are induced in the plasma donut being pushed out of the gun with the $\mathbf{J} \times \mathbf{B}$ force. At last, once a donut shaped blob separates from the rest of the plasma in the gun and initial reconnection is completed, newly born spheromak relaxes into the force-free equilibrium in the "flux conserver", a copper cylinder which confines the magnetofluid in SSX.
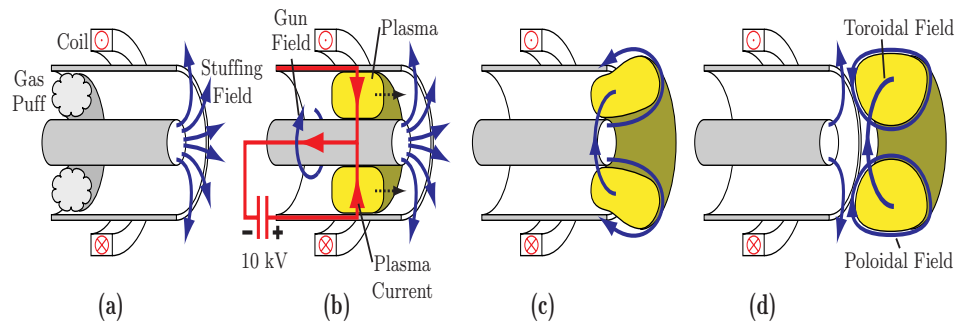

Figure 2: Formation of a spheromak in a magnetized coaxial plasma gun.

We use a symmetric set up in order to form two spheromaks and then observe the

processes taking place during their merging and reconnection. The schematic of the experiment is shown below. The conditions created in SSX are, in fact, very similar to those in solar corona with electron temperature T_e near 20 eV and electron density n_e of about $10^{14}\ cm^{-3}$.

Although we use a Langmuir triple probe[17] and magnetic probes to collect initial information about the plasma, conducting reliable internal measurements of such short-lived and dynamically unstable structures as spheromaks turns out to be non-trivial. Interaction of the probes with plasma destabilizes the equilibrium and may disrupt and/or interfere with the very processes we attempt to measure. Furthermore, solely measuring plasma parameters at a few points inside the flux conserver does not provide one with enough information about the highly non-uniform environment of the experiment.
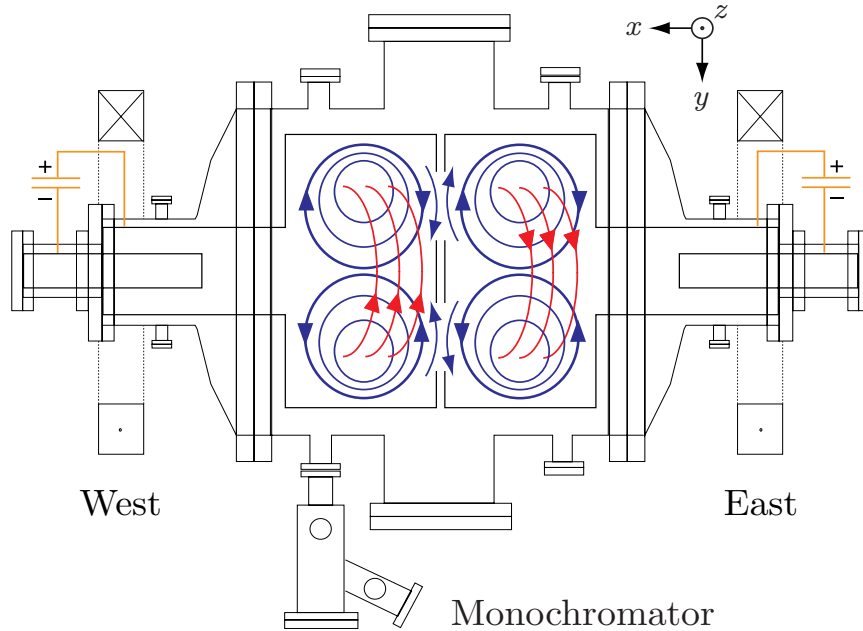
Figure 3: Formation of a spheromak in a magnetized coaxial plasma gun.

We are thus forced to turn to making external measurements, detecting light emitted by impurities in the spheromak plasmas and highly energetic ions accelerated in the reconnection region of the flux conserver. These diagnostic do not disturb plasma but integrate signal over a volume contained in a narrow cone around the "line of sight". As such, they provide us with values for plasma parameters averaged over that volume. Non-uniformity of the plasma once again limits usefulness of such measurements.

The obstacles one faces in trying to describe and understand both global and local dynamics of the spheromaks using diagnostics alone makes it only natural to attempt to model the experiment by adopting already existing resistive MHD codes such as TRIM.[26] In order to be able to extract information about the plasma itself from the external measurements,

we have to use simulation codes specific to the parameters being measured. To that end we employ the 0-D time-dependent coronal equilibrium impurity emission model, written by the author, to predict electron temperature and density in plasma from the impurity emission level. A trajectory tracing particle code together with TRIM is also used to predict the configurations of electromagnetic fields in the flux conserver from the high energy particle data.[1][19]

We check the outcomes of these simulations against the results of the measurements described above and can thus gain a better understanding of the processes occurring in the experiment.

This thesis is organized into four sections and five appendices. The introduction is followed by a description of the VUV spectroscopy project in Section 2. Experimental setup, data, model, and analysis are presented. Section 3 contains a brief introduction to resistive MHD followed by a discussion of specifics of the simulation and description of the current results. Some conclusions and future directions on SSX are presented in Section 4.

The reader should not consider this thesis to be the final word on any of the experimental or computational projects described below. Rather, it should be thought of as a thorough progress report on several of the projects taking place in SSX.
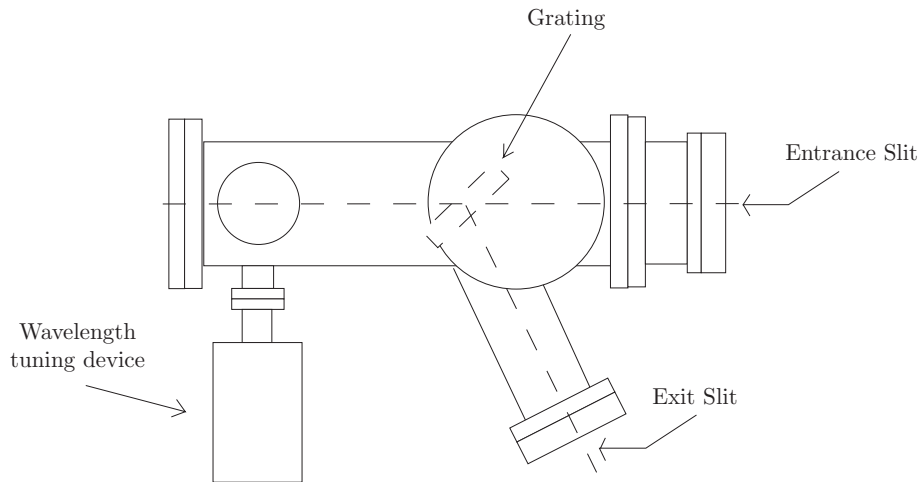
Figure 4: Schematics of the VUV monochromator.

2 VUV Spectroscopy

2.1 Experimental Setup and Calibration

We use a vacuum ultraviolet monochromator with nominal operational wavelength range of 50 nm to 560 nm to collect real time data from the experiment. The instrument has focal length of 0.2 meters and wavelength resolution of about 0.5 nm. The monochromator is supplied together with bilateral entrance and exit slits. These allow us to regulate both the overall amount of light entering the instrument through the entrance slit and the width of the intensity versus wavelength distribution of the light leaving the instrument through the exit slit. Grating is used to select and refocus a narrow bandwidth around the appropriate line out of the spectrum entering the monochromator on the exit slit. A sodium salicylate scintillator coated window on the exit end of the instrument is used for reemitting light below 250 nm.[25] The schematics of the monochromator is shown in Figure 4. See Figure 3 for the specific location of the monochromator on the flux conserver.

We register the light leaving the VUV monochromator with a high voltage PMT, which in turn relays the signal to a high frequency oscilloscope. Data is eventually stored on a computer hard drive making use of the developed data acquisition software.

Since the monochromator collects data at one wavelength setting at a time, the issue of calibrating the instrument with respect to the wavelength at which the measurements are taken is essential and non-trivial. Since we operate a vacuum instrument, we either have to introduce a known plasma source into the flux conserver in the line of sight of the monochromator or try to calibrate it through the window on the other side of the flux conserver. However, the first option is not presently available to us due to the excessive

costs associated with such a calibration, and even a quartz window, which we currently employ, only allows through the light of wavelengths above $\approx 180\,nm$. We are thus unable to get an independent calibration of the monochromator in the wavelength region between 50 nm and 180 nm, where most of the impurity lines of interest are located.

A mercury lamp was used to calibrate the instrument with respect to wavelength in the range of 250 nm – 550 nm. In order to complete the wavelength calibration, several scans covering most of the wavelength region between 50 nm and 250 nm were taken. The up-to-date wavelength calibration curve is presented in Figure 5. (See Appendix B for figures containing the results of the scans taken.)
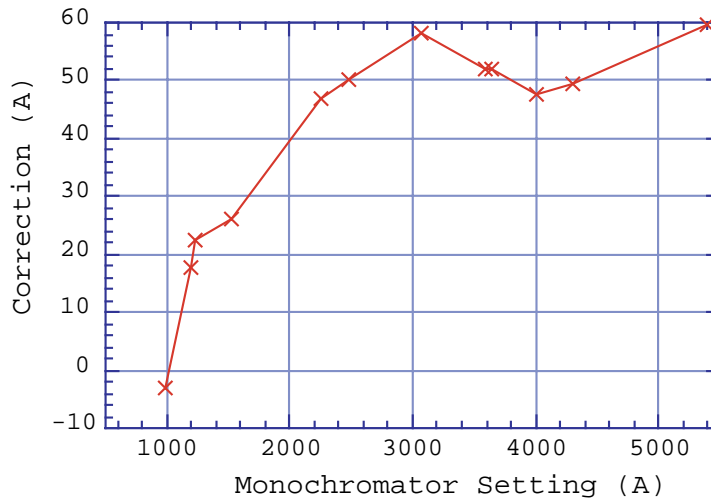
Figure 5: The VUV monochromator wavelength calibration curve.

The greatest contribution was observed to be from C III and C IV impurity ions with some emission from O III and O IV lines. A few of the apparent peaks in the emission spectrum are still not identified with any degree of certainty. A database of plausible impurity emission lines was put together based on the list of possible sources of impurities in the chamber and the expected range of values of the electron temperature T_e and the electron density n_e in the experiment. [1] (See Appendix A for the table of the considered impurity emission lines.)

An even greater problem is posed by the necessity of making an absolute intensity calibration of the VUV monochromator. Here, the plasma source itself has to be absolutely calibrated and the amount of light arriving at the entrance slit of the monochromator has to be known in order to calibrate the instrument. The second option is to use another already

---

[1]The expected sources of impurities and the elements are listed below:
Major sources: C, O;
Air: O, N, Ar;
Chamber: Cu, W, Fe, Ni, Cr;
Insulator: Al, O.

absolutely calibrated instrument in order to calibrate ours. However, neither of those options are currently available to us, once again, due to the excessive associated costs.

Thus, our ability to make conclusive statements about the state of plasma in the flux conserver solely from the time-evolution of the intensity of the impurity emission is presently limited by the inability to do an absolute intensity calibration of the VUV monochromator. Despite that, some conclusive statements about the state of plasma can still be made, as discussed below.

2.2 Experimental Data

Time resolved data from the following lines was recorded (see Figures 7 through 9 below for sample time series):

Impurity Lines	Outer Shell Configurations	Energy levels $E_i - E_k$ (cm^{-1})
C III 97.7 nm	$2s^2 - 2s2p$	0.00 - 102352.04
C III 124.7 nm	$2s2p - 2p^2$	102352.04 - 182519.8
C III 229.7 nm	$2s2p - 2p^2$	102352.04 - 145876.13
C IV 155.0 nm	$1s^2 2s - 1s^2 2p$	0.00 - 64591.7

Table 1: The impurity lines for which reliable data have been collected. Note that the initial and final configurations of the observed C III emission lines form a ladder such that the intensities of the 229.7 nm and 124.7 nm lines directly depend on the population of the upper energy level of the 97.7 nm transition (See Figure 6 below).

Typical time series of C III and C IV emission lines are observed to have two peaks. The first peak is seen to rise and fall relatively sharply with an approximate width of less than 10 μs. The second peak is observed to be significantly broader typically lasting for about $20 - 30$ μs.

A simple computational procedure was put together to identify the magnitude and timing of peaks in the emission data (See Table 2). These allow us to better identify impurity lines as well as provide the necessary statistics for comparing the data with predictions of the 0-D time-dependent impurity emission model. (See Appendix B for the code.)

Impurity Line	Time of peak 1, μs	Time of peak 2, μs	Peak1/Peak2 ratio
C III 97.7 nm	32.97 ± 0.74	48.92 ± 1.78	1.49 ± 0.30
C III 124.7 nm	32.89 ± 1.11	49.04 ± 2.30	2.11 ± 0.83
C III 229.7 nm	32.94 ± 0.76	48.67 ± 1.54	2.59 ± 0.61
C IV 155.0 nm	35.06 ± 1.58	48.40 ± 2.20	0.67 ± 0.37

Table 2: Timing and the ratios of magnitudes of the observed peaks in the recorded impurity emission time series. The values above were determined by averaging over 15 data runs for each emission line.

The line intensity ratio of the 229.7 nm line to the 97.7 nm line is calculated for both peaks:

$$I_{229.7}^1 / I_{97.7}^1 = (3.68 \pm 0.92)10^{-1}$$
$$\text{and}$$
$$I_{229.7}^2 / I_{97.7}^2 = (2.24 \pm 0.62)10^{-1}.$$

No such data for the 124.7 nm C III line is presently available.

The nearly exact match in the timing of peaks for the C III lines and the delay of the first peak for the C IV line serve as a confirmation that the peaks have been correctly identified and improve our knowledge of the wavelength calibration of the monochromator in the region above $100\ nm$. (Note that it takes longer to strip an atom of three rather than two electrons.) All three of the C III emission lines are observed to have very stable waveforms. A very small deviation in the timing of the peaks, in particular of the first peak, make them very useful for the subsequent analysis. On the other hand, the shape of the C IV emission line time series is seen to be much more dependent on a particular data run. Also note that the 97.7 nm C III line, being the resonant transition (i.e. it is the downward transition from the lowest lying excited state to the ground state), has twice as low variation in its magnitude ratio as the 124.7 nm and 229.7 nm C III lines, which are transitions between excited states and thus require higher values of the plasma parameters to have a significant level of emission intensity.

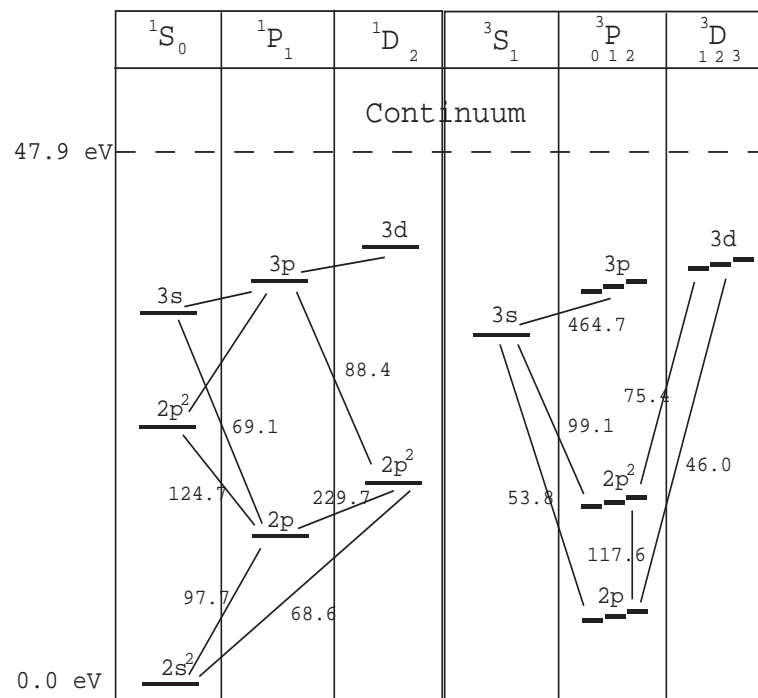**Figure 6:** Term scheme for C III ion. Transition wavelengths shown on the diagram are given in nanometers.
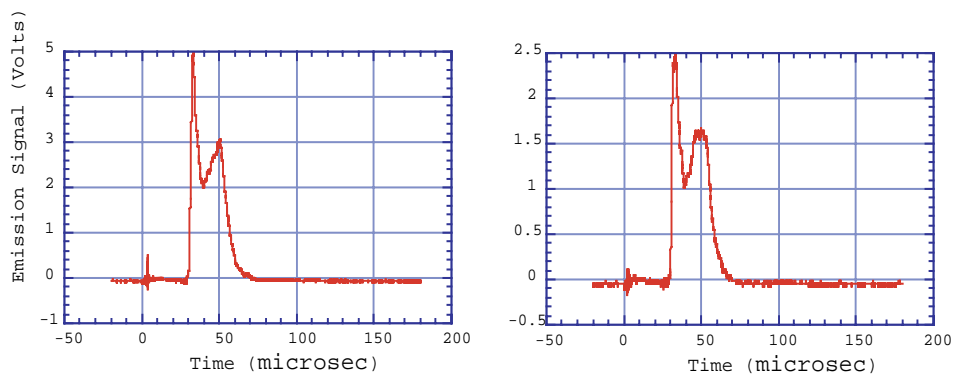
Figure 7: Typical monochromator time series for the C III 97.7 nm line.
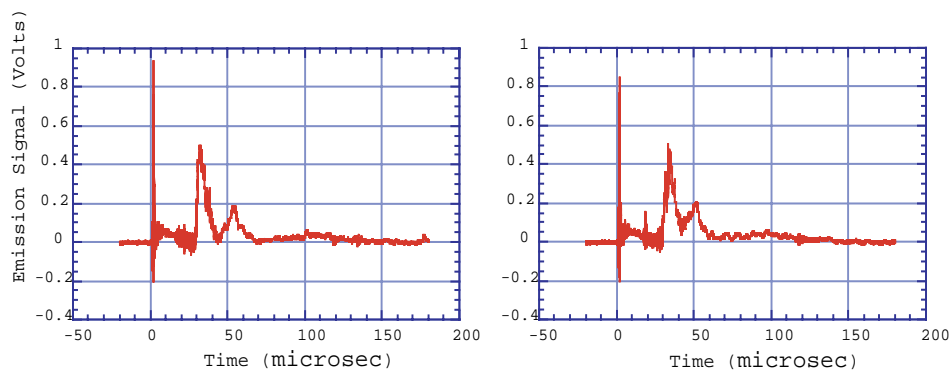

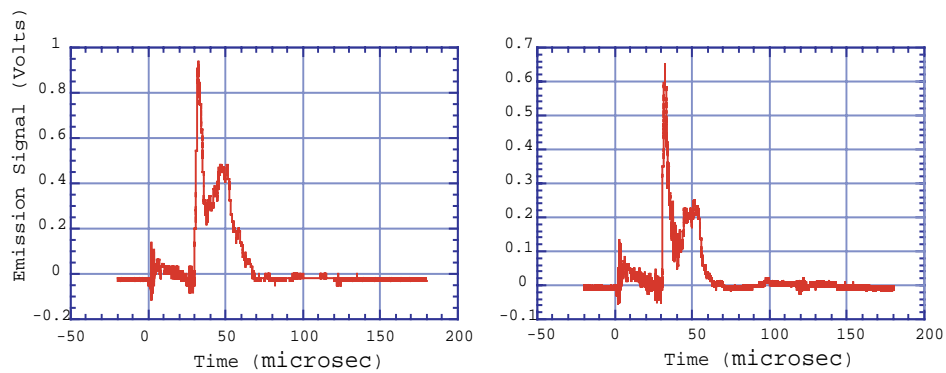**Figure 8:** Typical monochromator time series for the C III 124.7 nm line.

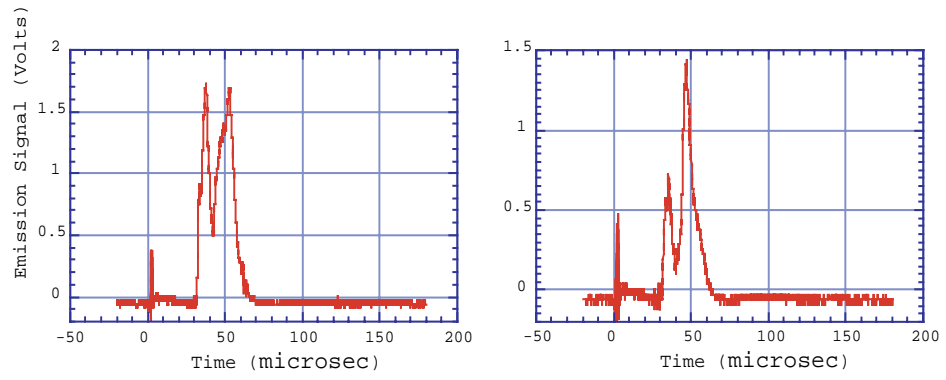**Figure 9:** Typical monochromator time series for the C III 229.7 nm line.

12

Figure 10: Typical monochromator time series for the C IV 155.0 nm line.

2.3   O-D Time-Dependent Coronal Equilibrium Model

We construct a model designed to simulate the time evolution of the population of different excitation states of impurity ions observed to be present in SSX plasmas. Once the population distribution is estimated, the intensity of the emission from the radiative downward transitions de-exciting the ions can be calculated and compared with the data collected with the VUV monochromator.

Both ionization/recombination and excitation/de-excitation processes strongly depend on both electron temperature T_e and electron density n_e of plasma. (See Appendix C for a quick review of the relevant ionization/recombination and excitation/de-excitation processes.) And these, in turn, govern the time evolution of the population of both different ionization and excitation levels. Thus, by finding time series for T_e and n_e such that the *calculated* time series of intensity $I_i^c(t)$ of the ith impurity emission line matches the *measured* intensity time series $I_i^m(t)$, we would be able to determine the actual time evolution of T_e and n_e in the experiment.

Note that the VUV monochromator used for collecting the emission data effectively integrates all the light emitted by the impurity ions in its line of sight. Therefore, the data contains no spatial resolution and therefore the model is developed to be "0-D" under the assumption of plasma being homogeneous in the line of sight of the instrument.

Analytic methods have been developed to calculate electron temperature and density from the impurity emission line ratios when plasma is in the state of local thermodynamic equilibrium (L.T.E.), which is achieved when the collisional transitions between different excitation levels of ions dominate the radiative transitions.[13][17][23] The distribution of state populations in L.T.E. is characterized by the Boltzmann distribution and the ratio of populations of any two excitation levels is given by the Boltzmann factor

$$\frac{N_i}{N_j} = e^{-(E_i - E_j)/T},\tag{1}$$

where N_i is the population of the ith excitation level, E_i is its energy and T is the temperature of the system. The "rule-of-thumb" condition for determining whether or not plasma has reached L.T.E. has been calculated by Griem [11] to be

$$n_e \geq 9 \times 10^{17} \left(\frac{\Delta E}{\chi}\right)^3 \left(\frac{T}{\chi}\right)^{1/2} \ [cm^{-3}],\tag{2}$$

where ΔE is the energy difference between two excitation states (or an excitation and a ground state) of an ion, and χ is its ionization energy.

SSX plasmas are optically thin (i.e. very little radiation is absorbed and most of the photons escape without interacting with plasma) and are known to lie in the T_e range of about 10 eV to 50 eV and have n_e on the order of 10^{14} (cm^{-1}).[2] Then, applying Eq. 2 to the resonant 97.7 nm C III emission line with $T_e = 20\,eV$, we have $n_e \geq 1 \times 10^{16}\,cm^{-3}$, which is one or two orders of magnitude greater than the observed range of electron densities on

---

[2]Measurements of T_e and n_e have been taken in the past with a Langmuir triple probe.

SSX. Thus, we are forced to abandon L.T.E. and resort to the so called time-dependent coronal equilibrium approximation, which acquires its name from the applicability to the solar corona.[20][6]

Here, the time evolution of different ionization stages of a given atom is considered, while steady state equations are solved for the population of different excitation levels of a given ion. This is justified since the relaxation time for the excitation/de-excitation processes τ_e is characterized by the inverse of the fastest transition rate between two levels $\tau_e = 1/A_{ij} \approx 10\ ns$, while the relaxation time for the ionization/recombination processes τ_i is the inverse of the radiative recombination rate. In the parameter range of the experiment, $\tau_i \approx 50\ \mu s$ and $\tau_i \gg \tau_e$.[13] Similarly, a Maxwellian distribution of electron velocities is assumed since in the SSX parameter range the relaxation processes for electrons have characteristic time on the order of 10 ns.[28][27]

Following Suckewer[28] and Hutchinson[13], we ignore dielectronic autoionization (the opposite of dielectronic recombination) since in the temperature range of the experiment the rate of atom-ion collisions is dominated by the electron-ion collision rate, which determines the electron impact ionization cross-section. Also, photo-excitation is neglected since plasma is optically thin and photons escape without interacting with the impurity ions.

The rate of change of population of the ith ionization stage n_i of a given atom is thus given by:

$$\frac{dn_i}{dt} = n_e(n_{i-1}\langle\sigma_{ci}v\rangle_{i-1} - n_i\langle\sigma_{ci}v\rangle_i +$$
$$n_{i+1}\langle\sigma_{rr}v\rangle_{i+1} - n_i\langle\sigma_{rr}v\rangle_i + n_{i+1}\langle\sigma_{der}v\rangle_{i+1} - n_i\langle\sigma_{der}v\rangle_i), \tag{3}$$

where $\langle\sigma_{ci}v\rangle_i$ is the collisional ionization rate, $\langle\sigma_{rr}v\rangle_i$ is the radiative recombination rate and $\langle\sigma_{der}v\rangle_i$ is the dielectronic recombination rate from the ith ionization level of a given atom, as defined in Appendix C. Note that in calculating the impact ionization and radiative recombination rates only the ground states of ions are considered due to their dominant population.[13] Then, in order to follow the time-evolution of the population of the ionization levels of a given atom, a system of $Z+1$ such differential equations is solved, where Z is the atomic number of the atom. A matrix method proposed by Carolan and Piotrowicz[6] is used to solve the system of equations with the Matlab software package (See Appendix for the code).

Since the excitation/de-excitation rates are assumed to be in the steady state balance, for each excitation level j of a given ion its population N_j has to satisfy the following:

$$\sum_{k<j} n_e N_k \langle\sigma_{kj}v\rangle_{ce} + \sum_{k>j} N_k A_{kj} + \sum_{k>j} n_e N_k \langle\sigma_{kj}v\rangle_{cde} =$$
$$\sum_{k>j} n_e N_j \langle\sigma_{jk}v\rangle_{ce} + \sum_{k<j} N_j A_{jk} + \sum_{k<j} n_e N_j \langle\sigma_{jk}v\rangle_{cde}, \tag{4}$$

where $n_e\langle\sigma_{kj}v\rangle_{ce}$ is the collisional excitation rate from the kth to the jth excitation level, A_{kj} is the spontaneous radiative de-excitation rate from the kth to the jth excitation level, and $n_e\langle\sigma_{kj}v\rangle_{cde}$ is the collisional de-excitation rate from the kth to the jth excitation level.

The cross sections of optically forbidden transitions are assumed to be negligible in comparison with the terms shown in Eq. 4.[28] Only several lowest lying excitation states are considered in the summations of Eq. 4 since only the ground and the first exited states are observed to have significant population for the range of plasma parameters relevant on SSX. The population of the metastable excited states of an ion is assumed to follow the Boltzmann distribution [28][18]

$$N_j \propto e^{-E_j/T_e}.$$

The populations of the relevant excitation levels are calculated by solving the system of simultaneous linear equations that result from applying Eq. 4 to every excitation level of a given ion. Simple vector algebra techniques are employed for doing so. (See Appendix for the implementation in Matlab.)

No diffusive impurity transport is included in the model, because the macroscopic variance of the plasma parameters and the overall dynamics of the spheromak plasmas are observed to be far more significant than local changes in impurity density, as discussed in Section 3.4.

2.4 Analysis of the Data with the Model

The upshot of the impurity emission project on SSX is to determine the time evolution of plasma parameters such as electron temperature T_e and density n_e in the experiment solely from the data collected with the VUV monochromator. This would be accomplished by comparing the line ratios of the intensities of the impurity emission lines taken from the data with the corresponding line ratios determined by the model described above for given values of T_e and n_e.

Two basic methods of analysis of the impurity emission data have been attempted.

2.4.1 Application of minimization techniques to the problem of time dependent parameter fitting

We attempt to approach the problem at hand as one of finding a local minimum of a multivariable single-valued function. In particular, we employ the simplex algorithm[24] to find the time-evolution of T_e and n_e by minimizing some function $g(t; T_e(t), n_e(t))$ with respect to the parameters T_e and n_e. The function g is defined as follows

$$g(t; T_e(t), n_e(t)) = \frac{I_i^c(t; T_e, n_e)}{I_j^c(t; T_e, n_e)} * \frac{I_j^m(t)}{I_i^m(t)} - 1, \qquad (5)$$

where $I_i^c(t; T_e, n_e)$ is the calculated intensity of the ith emission line at time t and $I_i^m(t)$ is the measured intensity of the ith emission line at time t. Note that the magnitude of $I_i^c(t; T_e, n_e)$ at $t = t_0$ depends on the time-evolution of $T_e(t')$ and $n_e(t')$ for all $t' \leq t_0$.

This method, is a very general one and can be used for determining the time evolution of the plasma parameters both from a line ratio of two emission lines belonging to the same ion and from a line ratio of two lines belonging to different ionization stages of the same atom. However, there are two significant problems that prevent us from presently using this algorithm.

The first one is of a fundamental nature. In order to complete the very first iteration of the algorithm, the initial distribution of the population of a given atom among its ionization levels has to be specified. The output of the algorithm turns out to be very sensitive to those initial conditions. However, the non-triviality of the physical processes occurring during the initial spheromak formation stage makes it very difficult to make reliable estimates of those input parameters. The second problem we face is of a more practical sort. Since the function g to be minimized is defined in terms of the line-ratios taken from the real data, the presence of the spheromak formation-related noise in the time series of the emission lines has a very strong effect on the output of the algorithm. And particularly so, when at least one of the lines considered is a relatively weak one (Ex. 124.7 nm C III line), thus making the formation noise comparable to the actual signal and significantly complicating the computational procedure of the algorithm.

Appendix D contains the detailed description of the algorithm and the routines used for its implementation in Matlab.

2.4.2 Analysis of timing and magnitude ratios of the peaks in the time evolution of the intensity of the measured impurity emission lines

We have to utilize specific details of the line intensity time series in order to make any conclusive statements about the state of plasma in the flux conserver during experimental runs.

As noted in Section 2.2, the currently available line intensity data from the 229.7 nm C III, 124.7 nm C III, 97.7 nm C III and 155.0 nm C IV lines have a two peak waveform. It would be reasonable to assume that such a shape is due solely to high electron temperature and density of plasma during the spheromak formation stage of an experimental run. It would follow that carbon first quickly "burns through" the C III and C IV ionization levels (i. e. most of the C III and C IV atoms are quickly further ionized), which results in the sharp first peak, and only later, when the plasma cools off and the electron density goes down, carbon ions recombine back and the broader second peak appears. However, this type of analysis would be correct if SSX plasmas were more homogeneous and less turbulent than they really are.

Presently, though, in order to understand and correctly interpret the data collected with the instrument, we have to carefully consider all the details of the experiment. It is essential that the line of sight of the monochromator does not go through the central part of the flux conserver. As shown in Figure 3, the VUV monochromator is not centered on the machine and thus cannot collect data from the main body of plasma once the spheromaks have detached themselves from the plasma guns.

Our present interpretation of the data is that the first peak observed in the time series of the C III lines is, in fact, carbon burning through the beryllium-like ionization level during the initial reconnection. However, it is our understanding that the decay of the first peak of the C IV line is in large part due to the hottest portions of plasma leaving the line of sight of the instrument, rather then simply burning through the third ionization level. We believe that the second peak in the time-histories of all three carbon lines observed is due to formation and slow relaxation of a spheromak in the flux conserver, so that only parts of the magnetic structure fall into the line of sight of the monochromator.

A careful analysis of the data confirms our understanding of the overall dynamics of plasma during a run. The reproducibility of the shape of the time-histories of the three C III lines together with much more significant variation in the shape of the time-history of the C IV line support the claim that the SSX plasma parameters are such that C IV is typically the highest ionization level reached by carbon atoms. The presence of a very well defined time delay of the first peak of the 155.0 nm C IV line with respect to the corresponding peak of the C III lines also supports the claim that the plasma initially burns through most of C III, while the breadth and matching timing of the second peaks is reflective of the relaxation processes taking place about 45 μs into the run. Large variation in the peak-to-peak ratio of the 124.7 nm and 229.7 nm lines of C III as compared to the variation in the peak-to-peak ratio of the 97.7 nm resonant C III line, as well confirm that the electron temperature and density of plasma are barely high enough to excite the higher lying $2p^2$ excitation levels of the C III ion.
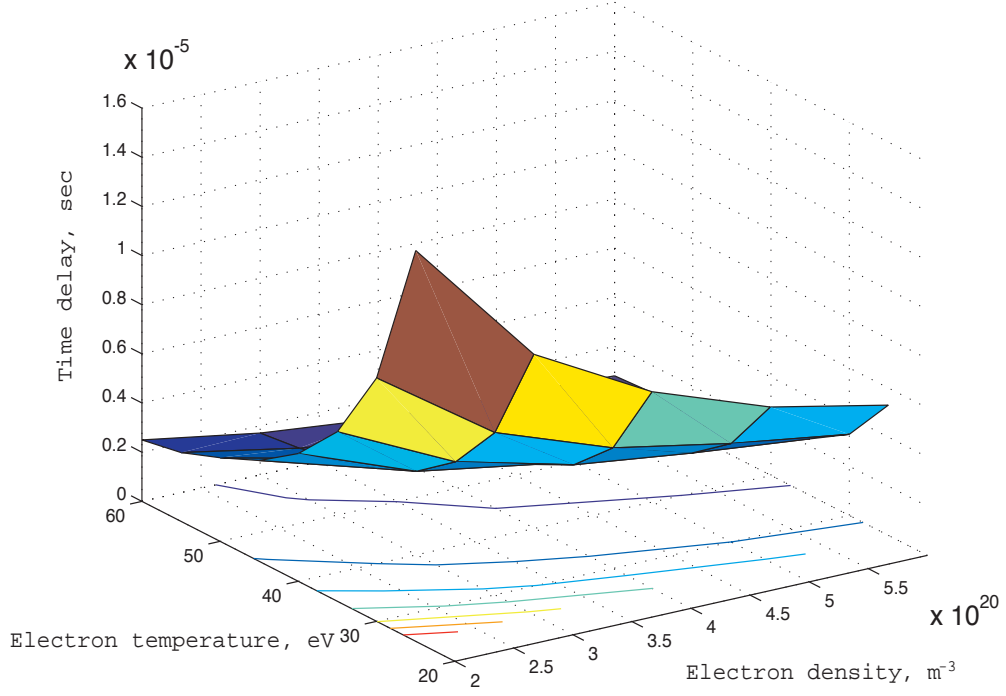
Figure 10: The 3-D color map demonstrates the time delay between the peaks in the time series of the 155.0 nm C IV and 229.7 nm C III lines predicted by the model as a function of both electron temperature T_e and electron density n_e. The contours in the $T_e \times n_e$ plane specify the values of T_e and n_e for which the time delay is $2 \ \mu s, 4 \ \mu s, ..., 14 \ \mu s$.

We use the modeling routines described in the previous section to narrow down the set of possible T_e and n_e values that could be occurring in the experiment, by taking advantage of the observed time delay $\Delta t \approx 2 \ \mu s$ between the peaks in the 155.0 nm C IV line and the 229.7 nm C III line time-histories. Figure 10 contains a 3-D color map demonstrating the predicted time delay between the peaks in the time-histories of the lines as a function of both electron temperature T_e and electron density n_e. As shown in Figure 10, we are able to narrow down the range of values in the $T_e \times n_e$ parameter space that could possibly be the SSX temperature and density parameter values to an almost linear relationship between T_e and n_e.

The ratios of line intensities of two transitions that belong to the same ion can also be used to obtain approximations for the plasma's parameter values.[29][30] In particular, we consider the line ratios of the following C III lines: 229.7 nm to 97.7 nm; and 124.7 nm to 229.7 nm. (See Figure 6 for the term diagram of C III.) Figure 11 and Figure 12 show model's predictions for those ratios in the section of interest in the parameter space.
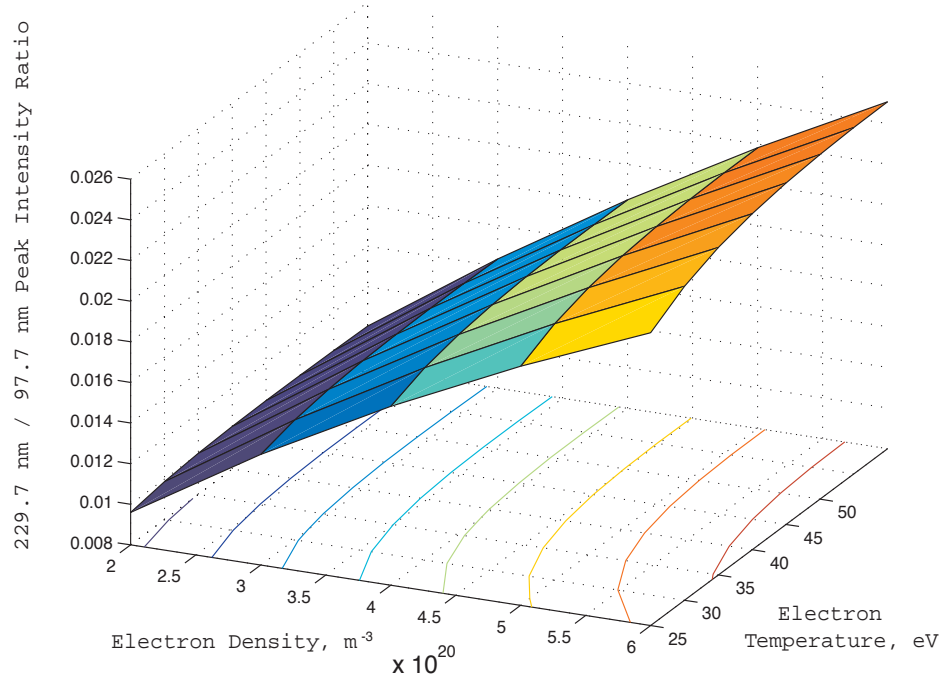
Figure 11: The 3-D color map demonstrates the line ratio of 229.7 nm and 97.7 nm C III lines predicted by the model as a function of both electron temperature T_e and electron density n_e. The contours in the $T_e \times n_e$ plane specify the values of T_e and n_e for which the ratio is 0.01, 0.012, ..., 0.024.

It is evident from Figure 11 that the line ratio of the 229.7 nm emission intensity to the intensity of the 97.7 nm line is predicted to be nearly independent of the electron temperature when the electron density is below 6×10^{20} m^{-3}. The results predict that the line ratio $I_{229.7} : I_{97.7}$ of these two lines should be about 1:40 in the parameter range of interest. The experimental data, however, suggest that the ratio is about 1:4, which is a factor of ten greater. As of now, no satisfactory explanation of such divergence between the data and the model have been found. Even though an absolute intensity calibration of the monochromator has not been conducted (see Section 2.1 for the discussion on the monochromator calibration), we do not expect that to influence the emission intensity data by more than a factor of two.

Unlike Figure 11, Figure 12 below demonstrates that the line ratio of the 124.7 nm emission intensity to the intensity of the 229.7 nm line is predicted to depend both on the electron temperature and the electron density of plasma and should be about 0.4 in the expected SSX parameter range. Unfortunately, no reliable data to either confirm or deny such claim is presently available.

We conclude that by combining the comparisons of the line ratios taken from experimental measurements with the corresponding model predictions of the impurity emission lines discussed above, one could determine both electron temperature and density of plasma
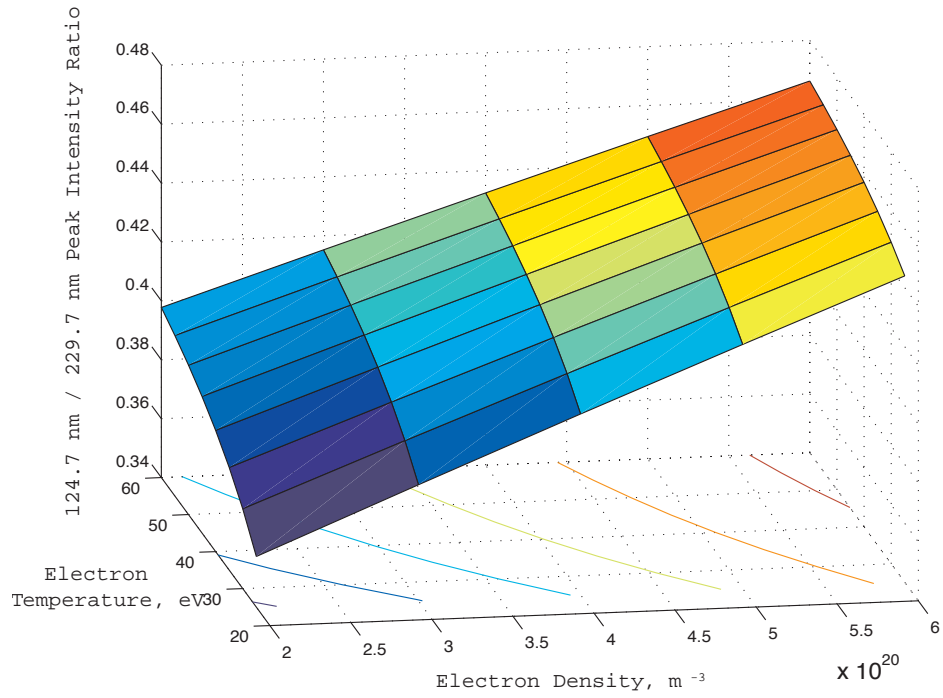
with a fair degree of certainty.

Figure 12: The 3-D color map demonstrates the line ratio of 124.7 nm and 229.7 nm C III lines predicted by the model as a function of both electron temperature T_e and electron density n_e. The contours in the $T_e \times n_e$ plane specify the values of T_e and n_e for which the ratio is 0.36, 0.38, ..., 0.46.

3 2-D Resistive MHD Simulation

3.1 Basic Theory of Resistive MHD Approximation for Plasma Interactions

To those unfamiliar with the subject, the field of plasma physics can appear to have been already exhausted many years ago. After all, plasma is just a very hot low density gas highly responsive to electromagnetic fields that permeate it. Thus, the basic physical laws that govern plasma behavior are Maxwell's equations and the kinetic laws of particle motion, both of which are well known. However, it is the combination of those physical laws as well as the number of particles that have to be considered that make the task of calculating the time evolution of plasma exactly absolutely impossible.

The hydrodynamic approximation of plasma is most commonly made and is valid for most of experimental plasmas.[5] Plasma is then treated as a single conducting fluid and we can write down the set of equations describing its time and space evolution:

$$\nabla \times \mathbf{E} = -\frac{\partial \mathbf{B}}{\partial t} \tag{6}$$

$$\nabla \times \mathbf{H} = \frac{\partial \mathbf{D}}{\partial t} + \mathbf{J} \tag{7}$$

$$\nabla \cdot \mathbf{D} = \sigma \tag{8}$$

$$\nabla \cdot \mathbf{B} = 0 \tag{9}$$

$$\rho \left[\frac{\partial \mathbf{u}}{\partial t} + \mathbf{u} \cdot \nabla \mathbf{u} \right] = \sigma \mathbf{E} + \mathbf{J} \times \mathbf{B} - \nabla P, \tag{10}$$

$$\frac{\partial \rho}{\partial t} + \nabla \cdot (\rho \mathbf{u}) = 0 \tag{11}$$

$$\frac{\partial \sigma}{\partial t} + \nabla \cdot \mathbf{J} = 0, \tag{12}$$

where Eq. 6 through Eq. 9 are the Maxwell's Equations for electromagnetic fields in a medium, Eq. 10 is the equation of motion of ordinary fluid plus the electromagnetic force term, Eq. 11 is the 'mass continuity equation' and Eq. 12 is the 'charge continuity equation' for the magnetofluid. When some kind of 'equation of state' (for example, the isothermal law $p = nT$) and the, so called, 'generalized Ohm's law' (Eq. 13), arising from the electron-ion interactions, are included, the resulting set of nine equations constitutes a full set of single-fluid equations[9]:

$$\mathbf{E} + \mathbf{u} \times \mathbf{B} = \eta \mathbf{J} + \frac{\mathbf{J} \times \mathbf{B} - \nabla p}{ne}. \tag{13}$$

Due to the assumption of quasineutrality of plasma (electron density n_e is approximated to be equal to the ion density n_i) some immediate simplifications of the above equations follow. It can be shown that terms that include the charge density σ, its time-derivative $\partial\sigma/\partial t$, or the displacement current $\partial\mathbf{D}/\partial t$ can be neglected in comparison with other terms in the corresponding equations above. Eq.8 can also be omitted from the set of relevant equations since the magnitude of σ, thus defined by the divergence of $\mathbf{D}$, turns out to be too small to be of any importance.[9]

The generalized Ohm's law is, then, left as the most complex in the remaining set of equations. However, for plasmas with fluid drift velocities on the order of ion thermal speed, one can show that the $\mathbf{J} \times \mathbf{B}$ and ∇p terms in Eq. 13 can be ignored. That condition is equivalent to saying that the scale-length of the plasma fluid motion L should be much larger than the ion Larmor radius r_{Li}, i.e. $r_{Li}/L \ll 1$. In that approximation, we use the simple form of the Ohm's law:

$$\mathbf{E} + \mathbf{u} \times \mathbf{B} = \eta\mathbf{J}. \tag{14}$$

Summarizing, the system of equations to be solved in the resistive MHD is as follows:

$$\nabla \times \mathbf{E} = -\frac{\partial\mathbf{B}}{\partial t} \tag{15}$$

$$\nabla \times \mathbf{B} = \mu_0\mathbf{J} \tag{16}$$

$$\nabla \cdot \mathbf{B} = 0 \tag{17}$$

$$\rho\left[\frac{\partial\mathbf{u}}{\partial t} + \mathbf{u}\cdot\nabla\mathbf{u}\right] = \mathbf{J} \times \mathbf{B} - \nabla P, \tag{18}$$

$$\frac{\partial\rho}{\partial t} + \nabla\cdot(\rho\mathbf{u}) = 0 \tag{19}$$

$$\nabla \cdot \mathbf{J} = 0, \tag{20}$$

where we assume $\mathbf{J}$ to include the magnetization of the plasma medium.

For the future reference, we should now define several parameters commonly used to characterize plasmas in the plasma physics community. The Alfvén velocity v_A is defined to be the hydromagnetic wave velocity of travel along the magnetic field lines and is the characteristic velocity at which perturbations of the force fields travel in plasma.[5] The Lundquist number S is defined to be the ratio of the $\mathbf{J} \times \mathbf{B}$ force to the resistive magnetic diffusion force and is, consequently, descriptive of the rate of diffusion of magnetic structures in plasma. Another dimensionless number β is defined to be the ratio of the thermal to the magnetic energy of plasma. It is characteristic of the strength of the plasma - B-field interactions.

3.2   2-D Cylindrically Symmetric Code – TRIM

We employ the 2-D cylindrically symmetric non-ideal MHD code – TRIangular Magnetohydrodynamics (MHD), by Schnack[26], to simulate the time-evolution of electromagnetic fields, momentum density and plasma density in SSX. In collaboration with W. H. Matthaeus and Gang Qui at Bartol Research Institute, we then attempt to use the time evolving electromagnetic fields to trace the trajectories of protons in SSX.[10]

Similar to the VUV spectroscopy project, we determine the relevant parameter range for the magnetic fields and mass density from the internal measurements, then run the simulations for different values of initial parameters in that range to determine the expected energies of ions leaving the flux conserver. Those calculations are, in turn, to be compared with the existing data of energetic ion flow, which has been externally measured.[14] Thus, we again hope to gain information about the time-evolution of crucial plasma parameters only making use of data from external measurements coupled with results of computer simulations.

TRIM solves the equations of resistive MHD, described in the previous section, in cylindrical geometry and finite volume. Cylindrical symmetry of the boundary conditions is assumed. Given such boundary conditions and initial configuration of electromagnetic fields, plasma density, pressure and momentum density, together with several constant parameters, such as the Lundquist number S, TRIM solves for the time evolution of the three components of the vector potential A, the three components of the momentum density $\rho\mathbf{v}$, the density ρ and the pressure P. The calculations are done on an unstructured adaptive grid of triangles in the $\hat{\mathbf{r}} \times \hat{\mathbf{z}}$ plane and a pseudospectral algorithm with fast Fourier transforms is used for the periodic toroidal ($\hat{\phi}$) direction.[26] Though TRIM can potentially be used with or without adaptive mesh, in several different thermodynamic modes and has multiple options for calculating resistivity and viscosity, here, we should limit ourselves to a discussion based only on the selections currently made for those options.
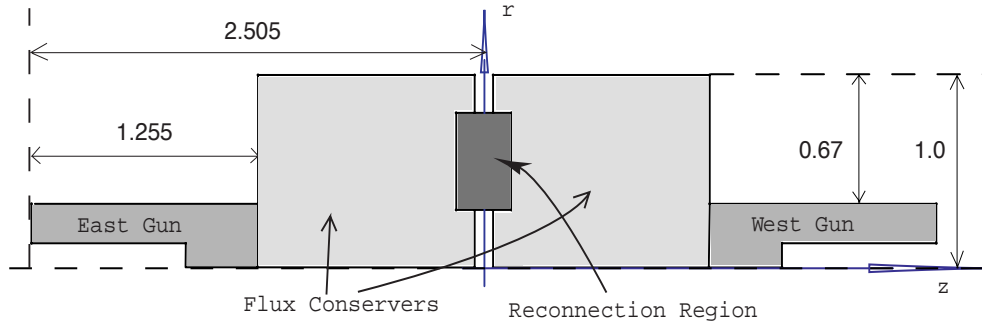

Figure 13: The layout for creating the grid of triangles on which all computations are made. z-axis is the axis of cylindrical symmetry. The mesh density is pre-assigned to be low in the flux conservers and a factor of 20 higher in the reconnection region. The specified dimensions are given in normalized units (See Section 3.3)

24

Since the simulation project is still very much in progress and only the first measurable results are being presented here, we have so far chosen to run TRIM with the simplest options available. The code is currently used on a fixed mesh (See Figure 13), in the isothermal mode (plasma density and pressure are equated) and with fixed and uniform viscosity and resistivity ($\eta = 1/S$). We choose a high density mesh in the reconnection region in order to be able to resolve small scale structures that result from the interaction of two spheromaks. The mesh density in the plasma guns is chosen to be intermediate between that of the flux conservers and of the reconnection region, as both too fine and too coarse computational grids in the guns give rise to instabilities during the formation stage of the spheromaks. All the edges of the layout except for $r = 0$ are assumed to be perfect conductors and special boundary conditions are implemented at $r = 0$ in order to avoid possible singularities.

The computational grid density, however, is not the only problem associated with using TRIM to simulate the spheromak formation stage of the experiment. As a reader familiar with plasma physics would note, the process of spheromak formation in SSX is highly non-MHD. (See Figure 2) As described in the previous section, external electric fields are ignored in the MHD approximation and we are thus forced to simulate the real spheromak formation process by some other MHD allowed processes in the simulation.

The configuration of fields used to initialize TRIM is currently composed of two separate effects. In order to create the poloidal stuffing B-field experimentally produced by an external magnetic coil, in TRIM, we assume existence of a solenoid in the inner rod of the plasma gun. The magnetic fields produced by such solenoid can successfully model the corresponding magnetic fields in the experiment. And, in order to compensate for the absence of voltage difference between the inner rod and outer walls of the plasma gun, a gradient in the z-direction of the toroidal magnetic field B_ϕ is introduced. So that by the Ampere's law:

$$J_r = -\frac{\partial B_\phi}{\partial z}. \tag{21}$$

Radial currents are, therefore, induced in the gun and then the $\mathbf{J} \times \mathbf{B}$ forces push the magnetofluid out of the plasma gun, as in the experimental setup. It should be noted that the timing of the experimental and computational spheromak formation methods can disagree considerably due to fundamental physical difference between an introduction of gradient toroidal magnetic fields into existing magnetofluid and an ionization of neutral hydrogen gas with a high voltage discharge.

One of the greatest challenges faced by the author in the attempts to reproduce the experimental process of the spheromak formation under the restrictions of resistive MHD was to prevent the code from generating small scale instabilities in the regions of low plasma density and high poloidal magnetic field right outside of the plasma guns. These problems were eventually overcome by introducing low levels of "background density" in the flux conserver (about 1% - 5% of the volume averaged plasma density), while the rest of the mass density is initially placed in the plasma guns in such a way that the density level gradually decays from its peak value in the middle of the gun to the background density level at the gun opening.

3.3 Normalization of TRIM variables

It is customary in computational physics to apply certain normalization to the code variables used, so as to avoid dealing with values other than those of order unity as much as possible. When either too large or too small number quantities are introduced in iterative algorithms, it does not only slow down the calculations but might also cause propagation of round-off errors, which, in turn, grow into significant errors in the results and/or disrupt the calculations altogether.[16]

The particular normalization chosen by an author of a code are often related to specific applications, the author anticipates his/her code to be used for. Thus, when such codes are adapted for use under similar but, maybe, not the exactly expected conditions, some re-normalization of the code may be necessary. Such is the case with TRIM. The normalization procedure of comparing the physical resistive MHD evolution equations with those used by D. D. Schnack *et al* is presented below.

We should write all physical variables, operators and characteristic constants (ex. $\mathbf{B}, \nabla, S$) as a product of a code variable (operator) and a unit normalization constant. For example:

$$\mathbf{B} = \mathbf{B}' * B_0$$
$$\nabla = \nabla' * \frac{1}{L_0}$$
$$S = S' * S_0$$

Lets now compare the physical equations with the ones found in TRIM. From the Maxwell's equations we have for the electric field:

$$\mathbf{E} = -\mathbf{v} \times \mathbf{B} + \eta\mathbf{J} = -\mathbf{v} \times \mathbf{B} + \frac{\mu_0 L_A v_A}{S}\mathbf{J} =>$$

$$\mathbf{E}' * E_0 = -(\mathbf{v}' \times \mathbf{B}') * (v_0 * B_0) + \frac{\mathbf{J}'}{S'} * \frac{\mu_0 L_A v_A J_0}{S_0}. \tag{22}$$

(Note, here v_A and L_A have experimentally measured values). However, the code solves:

$$\mathbf{E}' = -\mathbf{v}' \times \mathbf{B}' + \frac{\mathbf{J}'}{S'}. \tag{23}$$

(Eq. 23 is true for the case when plasma resistivity is assumed to be uniform such that $\eta' = 1/S'$ (*Assumption 1*)). Then, dividing Eq. 22 through by E_0 and identifying like terms in the two equations above, we have

$$\frac{v_0 B_0}{E_0} = 1 \tag{24}$$

and

$$\frac{\mu_0 L_A v_A J_0}{v_0 B_0 S_0} = 1. \tag{25}$$

We solve for the current density from the magnetic fields:

$$\mathbf{J} = \frac{1}{\mu_0} \nabla \times \mathbf{B} => \mathbf{J}' * J_0 = \nabla' \times \mathbf{B}' * \frac{B_0}{\mu_0 L_0}. \tag{26}$$

And the code solves

$$\mathbf{J}' = \nabla' \times \mathbf{B}'. \tag{27}$$

Again, dividing Eq. 26 through by J_0 and comparing with Eq. 27, produces

$$\frac{B_0}{J_0 \mu_0 L_0} = 1. \tag{28}$$

Then, combining Eq. 25 and Eq. 28, we have

$$\frac{L_A v_A}{L_0 v_0} = S_0. \tag{29}$$

We calculate B-fields from the vector potential using

$$\mathbf{B} = \nabla \times \mathbf{A} => \mathbf{B}' * B_0 = \nabla' \times \mathbf{A}' * \frac{A_0}{L_0}. \tag{30}$$

And the code has

$$\mathbf{B}' = \nabla' \times \mathbf{A}'. \tag{31}$$

Dividing Eq. 30 through by B_0 and combining with Eq. 31 produces

$$\frac{A_0}{B_0 L_0} = 1. \tag{32}$$

We now use the ideal gas law

$$pV = nkT => p = \frac{\rho}{m_p} kT => p' * p_0 = \rho' * \rho_0 \frac{kT}{m_p}. \tag{33}$$

Consider the isothermal case (*Assumption 2*):

$$p' = \rho'. \tag{34}$$

Dividing Eq. 33 through by p_0 and combining with Eq. 34 produces

$$\frac{\rho_0}{p_0} * \frac{kT}{m_p} = 1. \tag{35}$$

For the moment density we have

$$\frac{\partial (\rho \mathbf{v})}{\partial t} = -\nabla \cdot \left(\rho \mathbf{v} \cdot \mathbf{v} - \frac{\mathbf{BB}}{\mu_0} + \left(p + \frac{B^2}{2\mu_0} \right) \right) =>$$

27

$$\frac{\partial(\rho'\mathbf{v}')}{\partial t'} = -\nabla' \cdot \left(\rho'\mathbf{v}' \cdot \mathbf{v}' - \left(\mathbf{B}'\mathbf{B}' - \frac{B'^2}{2} \right) * \frac{B_0^2/\mu_0}{\rho_0 v_0^2} + p' * \frac{p_0}{\rho_0 v_0^2} \right), \quad (36)$$

and the code implements the following

$$\frac{\partial(\rho'\mathbf{v}')}{\partial t'} = -\nabla' \cdot \left(\rho'\mathbf{v}' \cdot \mathbf{v}' - \mathbf{B}'\mathbf{B}' + \frac{1}{2} \left(p' + B'^2 \right) \right). \quad (37)$$

Again, comparing the corresponding terms of the two equations we have

$$\frac{B_0^2/\mu_0}{\rho_0 v_0^2} = 1 \quad (38)$$

and

$$\frac{2p_0}{\rho_0 v_0^2} = 1. \quad (39)$$

Then, from Eq. 35 and Eq. 39 it follows that

$$\frac{m_p v_0^2}{2} = kT = T_e \ (eV) \ => v_0 = 13841.12\sqrt{T_e} \ (m/s). \quad (40)$$

Choose $B_0 = \langle B \rangle = 0.05 \ (Tesla)$ to be the average magnetic field strength measured in the flux conserver (*Assumption 3*). Then, from Eq. 24

$$E_0 = v_0 B_0 = 13841.12\sqrt{T_e \ (eV)} * B_0 = 692.06\sqrt{T_e} \ (V/m) \quad (41)$$

Also, from Eq. 38 we have

$$\rho_0 = \frac{B_0^2/\mu_0}{v_0^2} = \frac{m_p}{2\mu_0} * \frac{B_0^2}{T_e \ (eV)} = (1.04/T_e) * 10^{-5} \ (kg/m^3) \ =>$$

$$\frac{\rho_0}{m_p} = (6.21/T_e) * 10^{21} \ (m^{-3}). \quad (42)$$

Now fix $L_0 = L_A = 0.25 \ (m)$ (the major radius of the flux conserver) and $v_A = \langle B \rangle/(\mu_0 m_p \langle n \rangle)^{1/2} = 7.71 * 10^4 \ (m/s)$, where $\langle n \rangle = 2 * 10^{20} \ (m^{-3})$ is the average measured number density (*Assumption 4*). Then, from Eq. 29

$$\tau_0 = \frac{L_0}{v_0} = (1.81/T_e^{1/2}) * 10^{-5} \ (sec) \quad (43)$$

and

$$S_0 = \frac{v_A}{v_0} = 5.57/T_e^{1/2} \quad (44)$$

(Note, $\tau_A = L_A/v_A = 3.24 * 10^{-6} \ (sec)$).

And, at last, from Eq. 28, Eq. 32 and Eq. 39 it follows that

$$J_0 = \frac{B_0/\mu_0}{L_0} = 159154.9 \ (A/m^2), \quad (45)$$

$$A_0 = B_0 L_0 = 1.25 * 10^{-2} \ (W/m). \tag{46}$$

$$p_0 = \frac{\rho_0 {v_0}^2}{2} = 159154.9 \ (A/m^2), \tag{47}$$

In the table below we summarize the above discussion by presenting the relevant normalizing units as functions of temperature and calculating particular values for the case of $T_e = 20$.

Physical Quantity	Symbol	Value as a function of T_e	Value at $T_e = 20$
Vector potential	A_0	$1.25 * 10^{-2} \ (W/m)$	$1.25 * 10^{-2} \ (W/m)$
Magnetic Induction	B_0	$5.00 * 10^{-2} \ (Tesla)$	$5.00 * 10^{-2} \ (Tesla)$
Electric Field	E_0	$6.92 \ T_e^{1/2} * 10^2 \ (V/m)$	$3.10 * 10^3 \ (V/m)$
Current Density	J_0	$1.59 * 10^5 \ (A/m^2)$	$1.59 * 10^2 \ (A/m^2)$
Length	L_0	$2.50 * 10^{-1} \ (m)$	$2.50 * 10^{-1} \ (m)$
Pressure	p_0	$9.96 * 10^2 \ (Pascal)$	$9.96 * 10^2 \ (Pascal)$
Lundquist Number	S_0	$5.57/T_e^{1/2}$	1.26
Density	ρ_0	$(6.21 m_p/T_e) * 10^{21} \ (kg/m^3)$	$3.11 m_p * 10^{20} \ (kg/m^3)$
Time	τ_0	$(1.81/T_e^{1/2}) * 10^{-5} \ (sec)$	$4.05 * 10^{-6} \ (sec)$
Velocity	v_0	$1.38 \ T_e^{1/2} * 10^4 \ (m/s)$	$6.19 * 10^4 \ (m/s)$

Table 3: The normalization values presented here are the multiplicative factors that should be used to convert the values of TRIM variables to the values of the corresponding real physical quantities.

3.4 Current Results and Comparison with Experimental Data

As discussed in Section 3.2, the TRIM simulation code is presently running in its simplest variation, so that the calculations are done on a fixed triangulated grid, in the isothermal mode and with fixed and uniform viscosity and resistivity.

We have been able to produce simulation runs whose general development closely matches our understanding of the spheromak formation and equilibrium in SSX.[7] The time evolution of the magnetic energy density and plasma density both in the flux conserver and in the reconnection region have been calculated and are observed to be very similar to those measured experimentally. (See Figure 14 below.) Although the measured magnetic energy density is seen to be a factor of six greater than the magnetic energy density predicted by TRIM, the shapes of the corresponding time series are very similar. Thus, increasing the initial magnetic fields in the plasma gun in TRIM should correct for the present magnitude difference between the simulation and the experiment.
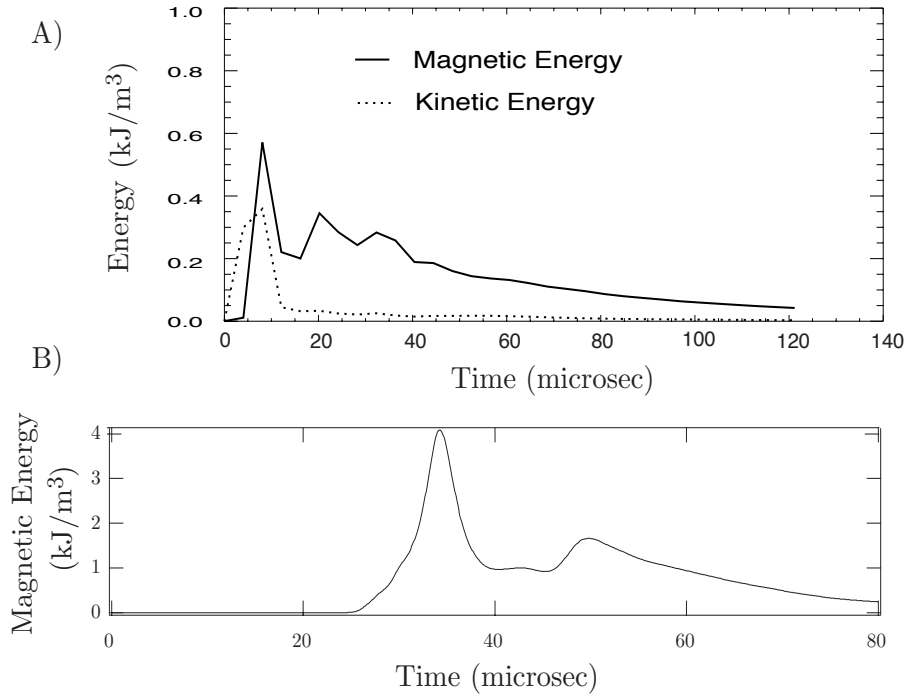

Figure 14: A) The time series of magnetic and kinetic energy densities, as calculated by TRIM, averaged over the volume of the flux conserver;
B) The time series of the magnetic energy density, as measured in the reconnection region of the SSX device.[3]

Figure 15 through Figure 17 demonstrate some of the magnetic configurations from the most recent TRIM simulation runs.

The similarity between the 2-D experimental data and the predictions of the simulation in Figure 15 is apparent. In either case, there appears to be, so called, O-point in the configuration of the magnetic fields.

The results of the TRIM simulation also support our interpretation of the VUV monochromator data, discussed in Section 2.4. As shown in Figure 17, a very dynamic initial formation stage is observed to be followed by much slower relaxation process, when spheromaks are formed and plasma is evenly distributed over the volume of the flux conservers. This confirms that it is necessary to consider the plasma dynamics while analyzing the impurity emission data with a 0-D code.

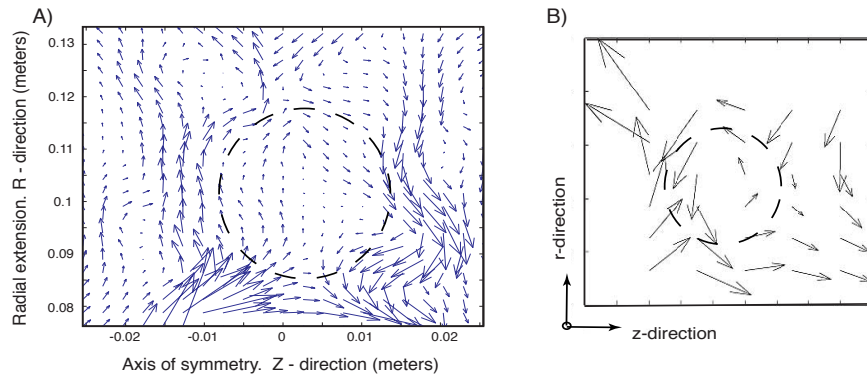**Figure 15: A)** The poloidal cross-section of the magnetic vector fields in the reconnection region during the spheromak formation stage of the TRIM simulation.
B) Experimental SSX data from 2-D magnetic probes taken in the reconnection region.[3]
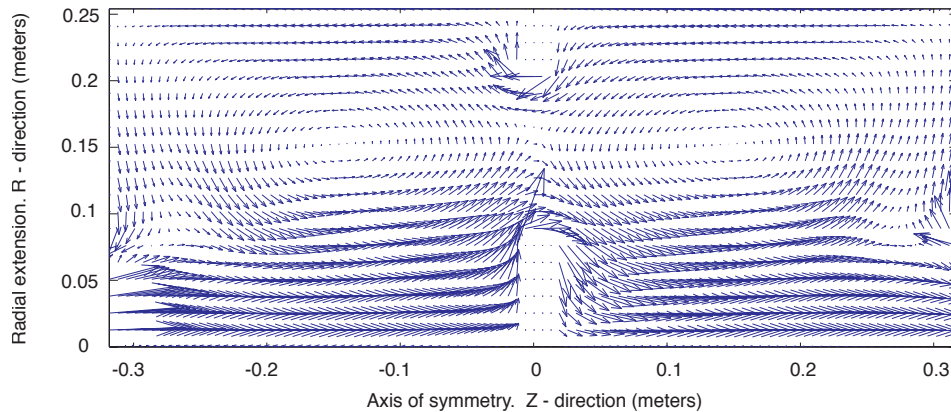
Figure 16: The poloidal cross-section of the magnetic vector fields in the flux conservers during the spheromak equilibrium stage of the TRIM simulation.

31

Z = -2.5*L₀

Z = 0

Z = 2.5*L₀

R = 0   R = L₀   R = 0   R = L₀   R = 0   R = L₀

Time = 1.0*τ₀ = 4.05 μs   Time = 3.0*τ₀ = 12.15 μs   Time = 5.0*τ₀ = 20.25 μs

Figure 17: A) Colormap of the magnetic flux during the spheromak formation stage.
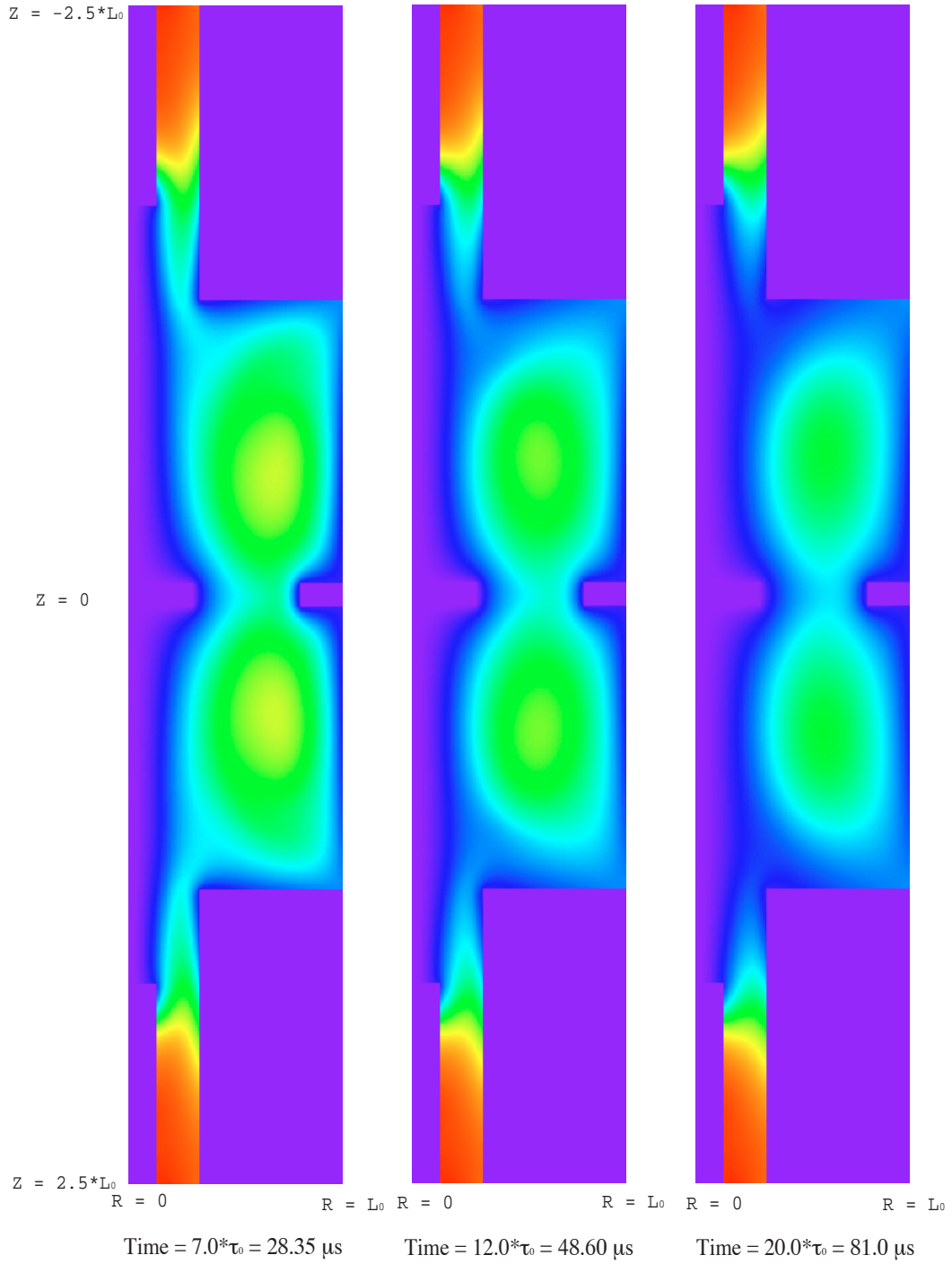
Figure 17: B) Colormap of the magnetic flux during the spheromak equilibrium stage.

The preliminary results from the application of the particle pushing code by Bill Matthaeus *et al* to the electromagnetic fields produced by TRIM are shown in Figure 18. In only a couple of μs, the particle energy distribution is observed to develop a long high energy tail. The few protons being accelerated are assumed to be the high energy ions observed with the particle detectors in SSX.[14]
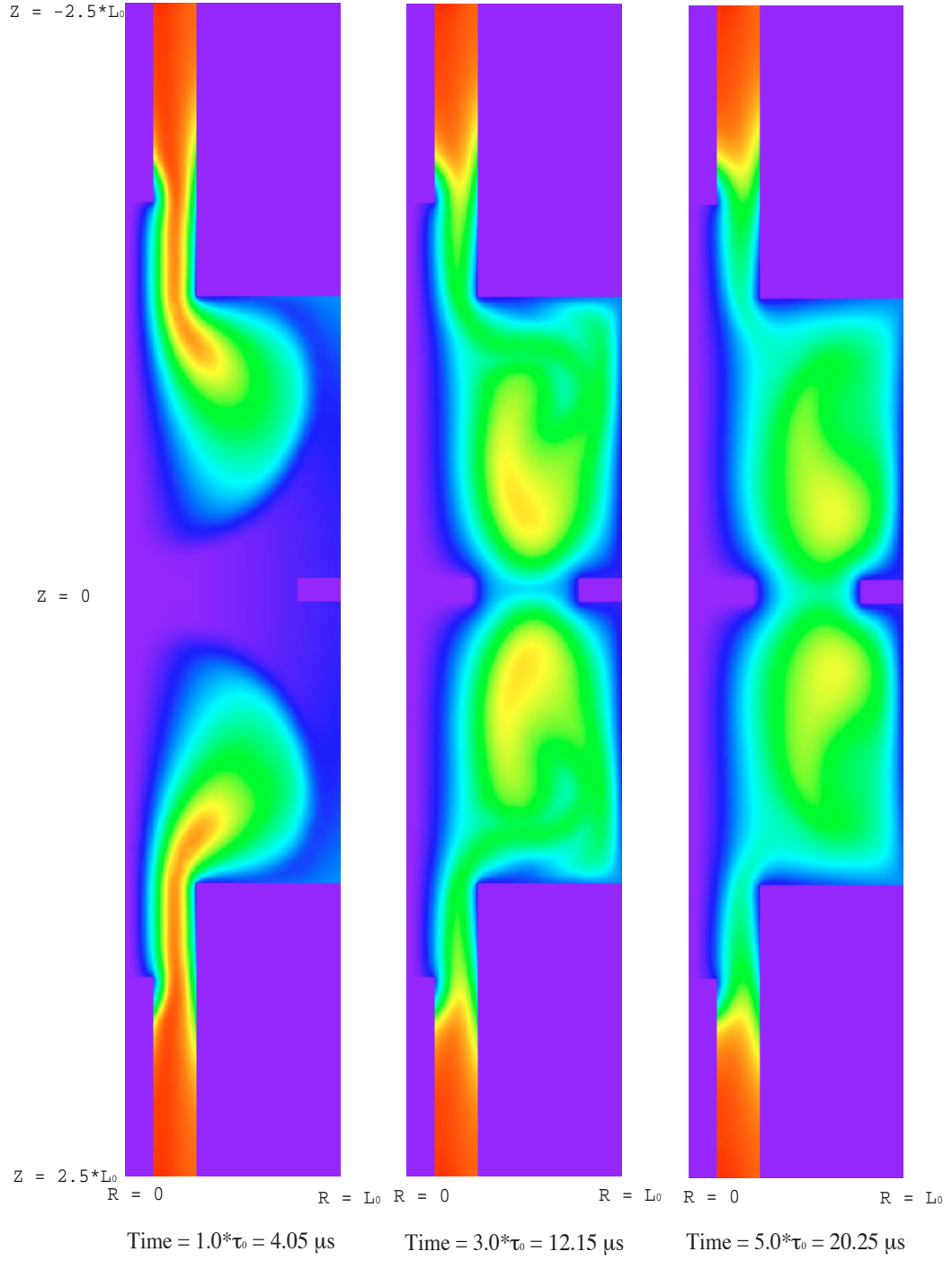

Figure 18: The time evolution of the energy distribution of a set of 1000 protons randomly placed into the TRIM predicted electromagnetic fields of the reconnection region in SSX. All protons have the initial velocity of 1, where both time and velocity are measured in the normalized TRIM units.

4   Future Directions on SSX

As was stated in Introduction and reinforced throughout this thesis, most of the projects described here have not yet lived the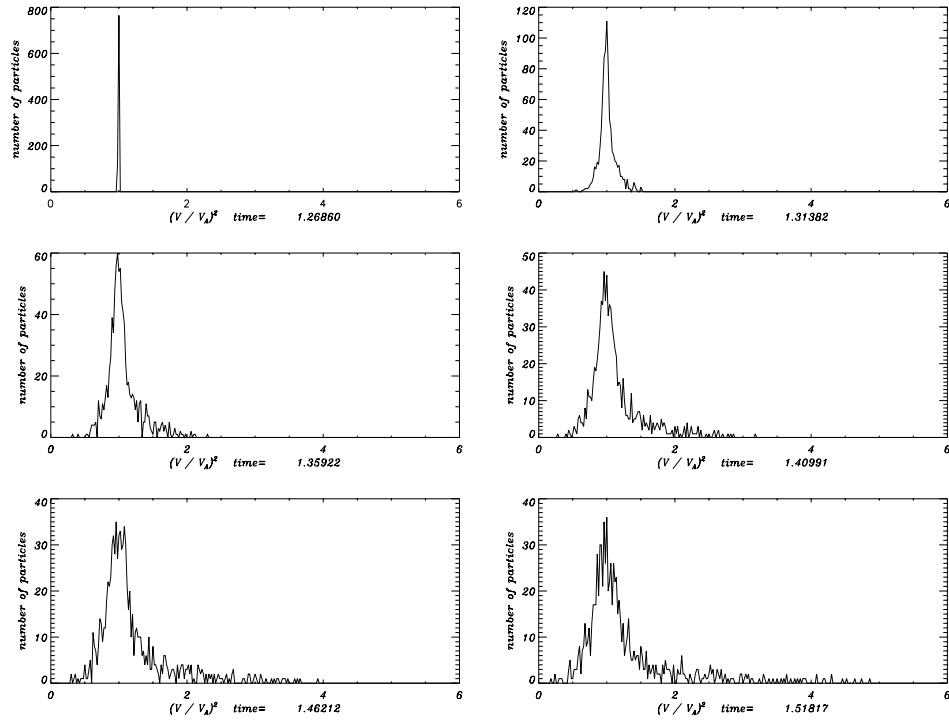ir life. For example, the absolute intensity calibration of the VUV monochromator is waiting to be done. Combining the plasma dynamics modeled by TRIM together with the predictions of the 0-D impurity emission code is also a possibility.

The very first data has recently been collected with a new triple Langmuir probe[15] (See Figure 19). Though some calibration and adjustments are still to be done, the initial data seems to be in good agreement with previous measurements and the predictions of the simulations described above. In particular, the recorded electron temperature time series seems to justify the assumption of constant temperature made in TRIM, while the observed peak in the electron density might serve as an explanation of the measured line intensity ratios from the plasma impurities.

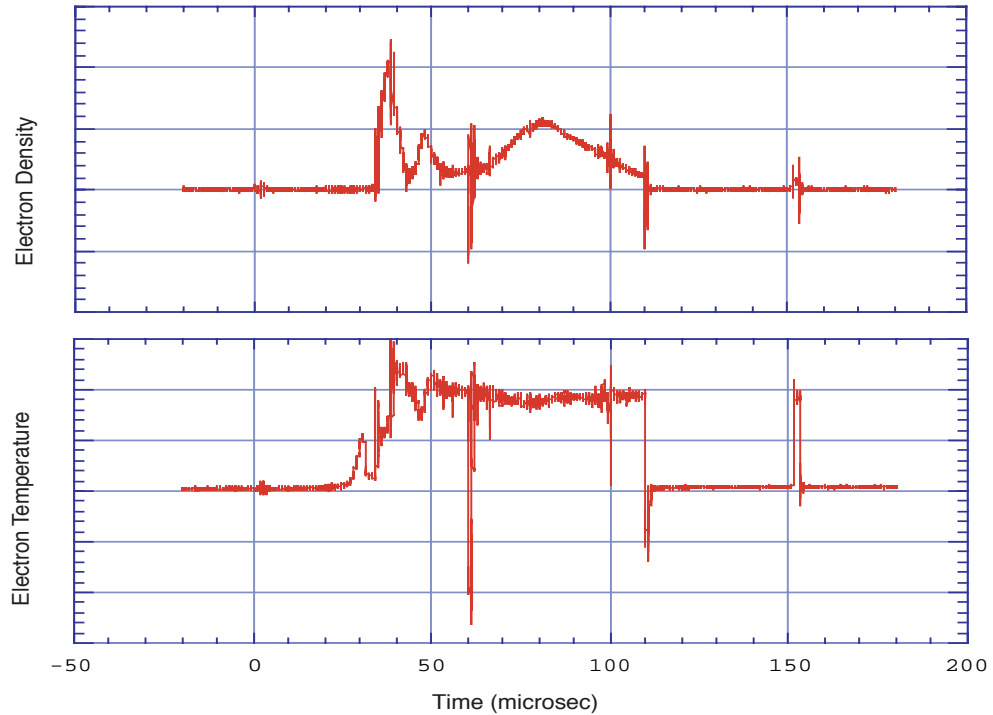**Figure 19:** The time evolution of the electron temperature and density as observed with a Langmuir triple probe. No scales on the T_e-axis and the n_e-axis are indicated, as absolute calibration of the probe is pending.

In collaboration with W. H. Matthaeus, a great effort is made to combine TRIM with the particle pushing code developed at Bartol Research Institute. The basic idea of the project

is to develop computational tools which would allow one to predict the magnetics in SSX purely from the ionic flow out of the flux conserver, and in particular from the reconnection region. To the date, measurements of ion flux of the Alfvenic and super-Alfvenic flow from the reconnection region has been successfully conducted.[3] (See Figure 20.) Good general agreement between these data and the preliminary particle pushing code results is observed (See Figure 18).
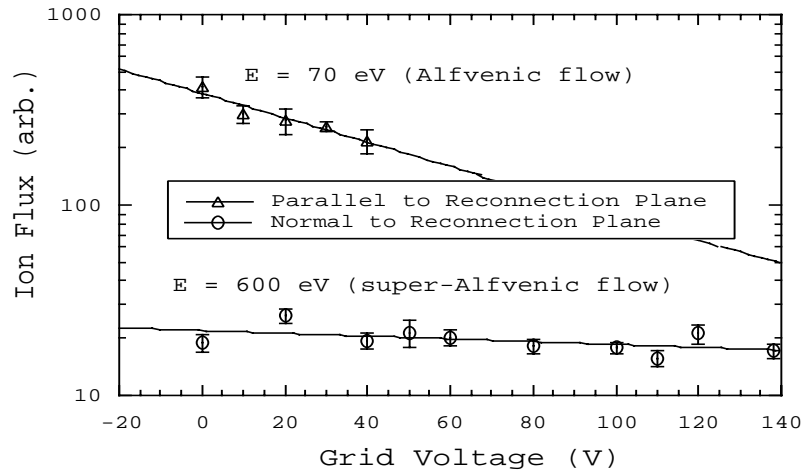
Figure 20: Retarding energy analyzer scan in SSX device. Top: merging spheromaks (in-plane), Alfvénic ions, $\bar{E}$ = 70 eV. Bottom: merging spheromaks (out-of-plane), super-Alfvénic ions, $\bar{E}$ = 600 eV.[3]

A $5 \times 5 \times 8$ magnetic probe set is in the final stages of assembly. The new forest probe will provide a time resolved 3-D B-field map of the reconnection region in SSX. With this new diagnostic, we hope to gain much better understanding of the physical processes that take place during the reconnection and are thought to be responsible for the acceleration of the super-energetic ions.

---

[3]Figure 19 is borrowed from a paper by M. R. Brown[3]

Appendix

A. Table of relevant transitions for considered ions.

Wavelength, A	$A_{ik}, 10^8 s^{-1}$	g_i - g_k	E_i - E_k, cm^{-1}	Configurations
C I				
2478.56	3.40e-01	1 - 3	21648.01 - 61981.82	$2s^2 2p^2 - 2s^2 2p3s$
1930.91	3.51e+00	5 - 3	10192.63 - 61981.82	$2s^2 2p^2 - 2s^2 2p3s$
1658.12	1.44e+00	5 - 3	43.40 - 60352.63	$2s^2 2p^2 - 2s^2 2p3s$
1657.91	3.43e+00	3 - 1	16.40 - 60333.43	$2s^2 2p^2 - 2s^2 2p3s$
1657.38	8.64e-01	3 - 3	16.40 - 60352.63	$2s^2 2p^2 - 2s^2 2p3s$
1657.01	2.52e+00	5 - 5	43.40 - 60393.14	$2s^2 2p^2 - 2s^2 2p3s$
1656.93	1.13e+00	1 - 3	0.00 - 60352.63	$2s^2 2p^2 - 2s^2 2p3s$
1656.27	8.58e-01	3 - 5	16.40 - 60393.14	$2s^2 2p^2 - 2s^2 2p3s$
1561.44	1.18e+00	5 - 7	43.40 - 64086.92	$2s^2 2p^2 - 2s 2p^3$
1561.34	2.94e-01	5 - 5	43.40 - 64090.95	$2s^2 2p^2 - 2s 2p^3$
1560.31	6.57e-01	1 - 3	0.00 - 64089.85	$2s^2 2p^2 - 2s 2p^3$
C II				
1335.71	2.84e+00	4 - 6	63.42 - 74930.10	$2s^2 2p - 2s 2p^2$
1335.66	4.74e-01	4 - 4	63.42 - 74932.62	$2s^2 2p - 2s 2p^2$
1334.53	2.37e+00	2 - 4	0.00 - 74932.62	$2s^2 2p - 2s 2p^2$
1323.95	4.49e+00	6 - 6	74930.10 - 150461.6	$2s 2p^2 - 2p^3$
1323.91	4.33e+00	4 - 4	74932.62 - 150466.7	$2s 2p^2 - 2p^3$
1066.13	1.63e+01	4 - 2	74932.62 - 168729.5	$2s 2p^2 - 2p^3$
1065.92	1.64e+00	4 - 6	74932.62 - 168748.3	$2s 2p^2 - 2p^3$
1065.89	1.47e+01	6 - 4	74930.10 - 168748.3	$2s 2p^2 - 2p^3$
1037.02	1.52e+01	4 - 2	63.42 - 96493.74	$2s^2 2p - 2s 2p^2$
1036.34	7.61e+00	2 - 2	0.00 - 96493.74	$2s^2 2p - 2s 2p^2$
904.48	1.37e+01	4 - 2	63.42 - 110624.17	$2s^2 2p - 2s 2p^2$
904.14	3.42e+01	4 - 4	63.42 - 110665.56	$2s^2 2p - 2s 2p^2$
903.96	2.74e+01	2 - 2	0.00 - 110624.17	$2s^2 2p - 2s 2p^2$
903.62	6.85e+00	2 - 4	0.00 - 110665.56	$2s^2 2p - 2s 2p^2$
858.56	2.35e+00	4 - 2	63.42 -116537.65	$2s^2 2p - 2s^2 3s$
858.09	1.18e+00	2 - 2	0.00 - 116537.65	$2s^2 2p - 2s^2 3s$
549.57	1.34e+00	4 - 2	63.42 - 182023.86	$2s^2 2p - 2s 2p3p$
549.51	3.35e+00	4 - 4	63.42 - 182043.41	$2s^2 2p - 2s 2p3p$
549.38	2.68e+00	2 - 2	0.00 - 182023.86	$2s^2 2p - 2s 2p3p$
549.32	6.71e-01	2 - 4	0.00 - 182043.41	$2s^2 2p - 2s 2p3p$
530.45	8.56e-01	4 - 4	63.42 - 188581.25	$2s^2 2p - 2s 2p3p$
530.36	5.14e+00	4 - 6	63.42 - 188615.07	$2s^2 2p - 2s 2p3p$
530.28	4.28e+00	2 - 4	0.00 - 188581.25	$2s^2 2p - 2s 2p3p$
C III				
4647.49	7.26e-01	3 - 5	238213.00 - 259724.3	$2s 3s - 2s 3p$
2296.87	1.38e+00	3 - 5	102352.04 - 145876.1	$2s 2p - 2p^2$
1247.383	2.08e+01	3 - 1	102352.04 - 182519.8	$2s 2p - 2p^2$

Wavelength, A	$A_{ik}, 10^8 s^{-1}$	g_i - g_k	E_i - E_k, cm^{-1}	Configurations
C III				
1176.37	5.47e+00	5 - 3	52447.11 - 137454.40	$2s2p - 2p^2$
1175.99	1.31e+01	3 - 1	52390.75 - 137425.70	$2s2p - 2p^2$
1175.71	9.86e+00	5 - 5	52447.11 - 137502.01	$2s2p - 2p^2$
1175.59	3.29e+00	3 - 3	52390.75 - 137454.40	$2s2p - 2p^2$
1175.26	4.39e+00	1 - 3	52367.06 - 137454.40	$2s2p - 2p^2$
1174.93	3.29e+00	3 - 5	52390.75 - 137502.01	$2s2p - 2p^2$
977.02	1.77e+01	1 - 3	0.00 - 102352.04	$2s^2 - 2s2p$
690.52	8.30e+00	3 - 1	102352.04 - 247170.2	$2s2p - 2s3s$
574.281	6.24e+01	3 - 5	102352.04 - 276482.8	$2s2p - 2s3d$
538.312	2.04e+01	5 - 5	52447.11 - 238213.00	$2s2p - 2s3s$
538.149	1.23e+01	3 - 3	52390.75 - 238213.00	$2s2p - 2s3s$
538.080	4.09e+00	1 - 3	52367.06 - 238213.00	$2s2p - 2s3s$
459.627	1.06e+02	5 - 7	52447.11 - 270014.74	$2s2p - 2s3d$
459.516	4.43e+01	3 - 3	52390.75 - 270010.83	$2s2p - 2s3d$
459.514	7.97e+01	3 - 5	52390.75 - 270011.93	$2s2p - 2s3d$
459.466	5.91e+01	1 - 3	52367.06 - 270010.83	$2s2p - 2s3d$
C IV				
1550.77	2.64e+00	2 - 2	0.00 - 64484.0	$1s^2 2s - 1s^2 2p$
1548.19	2.65e+00	2 - 4	0.00 - 64591.7	$1s^2 2s - 1s^2 2p$
1230.521	7.18e+00	4 - 2	320081.7 - 401348.1	$1s^2 3p - 1s^2 4s$
1230.043	3.59e+00	2 - 2	320050.1 - 401348.1	$1s^2 3p - 1s^2 4s$
1107.979	2.94e+00	4 - 4	320081.7 - 410336.1	$1s^2 3p - 1s^2 4d$
1107.930	1.76e+01	4 - 6	320081.7 - 410340.1	$1s^2 3p - 1s^2 4d$
1107.591	1.47e+01	2 - 4	320050.1 - 410336.1	$1s^2 3p - 1s^2 4d$
798.169	3.26e+00	4 - 2	320081.7 - 445368.5	$1s^2 3p - 1s^2 5s$
797.967	1.63e+00	2 - 2	320050.1 - 445368.5	$1s^2 3p - 1s^2 5s$
770.377	1.48e+00	4 - 4	320081.7 - 449888.2	$1s^2 3p - 1s^2 5d$
770.367	8.91e+00	4 - 6	320081.7 - 449889.9	$1s^2 3p - 1s^2 5d$
770.190	7.43e+00	2 - 4	320050.1 - 449888.2	$1s^2 3p - 1s^2 5d$
672.485	1.77e+00	4 - 2	320081.7 - 468784.0	$1s^2 3p - 1s^2 6s$
672.342	8.88e-01	2 - 2	320050.1 - 468784.0	$1s^2 3p - 1s^2 6s$
660.988	8.38e-01	4 - 4	320081.7 - 471370.3	$1s^2 3p - 1s^2 6d$
660.983	5.03e+00	4 - 6	320081.7 - 471371.5	$1s^2 3p - 1s^2 6d$
660.850	4.19e+00	2 - 4	320050.1 - 471370.3	$1s^2 3p - 1s^2 6d$
419.71	2.85e+01	4 - 2	64591.7 - 302849.0	$1s^2 2p - 1s^2 3s$
419.525	1.42e+01	2 - 2	64484.0 - 302849.0	$1s^2 2p - 1s^2 3s$
384.17	1.75e+02	4 - 6	64591.7 - 324890.3	$1s^2 2p - 1s^2 3d$
384.031	1.46e+02	2 - 4	64484.0 - 324879.8	$1s^2 2p - 1s^2 3d$
312.45	4.63e+01	2 - 2	0.00 - 320050.1	$1s^2 2s - 1s^2 3p$
312.42	4.63e+01	2 - 4	0.00 - 320081.7	$1s^2 2s - 1s^2 3p$
C V				
40.26	8.87e+03	1 - 3	0.00 - 2483371	$1s^2 - 1s2p$
34.97	2.55e+03	1 - 3	0.00 - 2859375	$1s^2 - 1s3p$

Wavelength, A	$A_{ik}, 10^8 s^{-1}$	g_i - g_k	E_i - E_k, cm^{-1}	Configurations
H I				
1215.6736	6.26e+00	2 - 2	0.00 - 82258.9206	$1s - 2p$
1215.6682	6.61e+00	2 - 4	0.00 - 82259.2865	$1s - 2p$
1025.7218	1.67e+00	2 - 2	0.00 - 97492.2130	$1s - 3p$
1025.7229	1.67e+00	2 - 4	0.00 - 97492.3214	$1s - 3p$
O I				
2972.29	7.54e-10	3 - 1	158.265 - 33792.583	$2p^4 - 2p^4$
1306.03	6.76e-01	1 - 3	226.997 - 76794.978	$2p^4 - 2p^3 3s$
1304.86	2.03e+00	3 - 3	158.265 - 76794.978	$2p^4 - 2p^3 3s$
1302.17	3.41e+00	5 - 3	0.00 - 76794.978	$2p^4 - 2p^3 3s$
1039.23	9.43e-01	5 - 3	0.00 - 96225.049	$2p^4 - 2p^4 4s$
988.77	2.26e+00	5 - 7	0.00 - 101135.407	$2p^4 - 2p^3 3s$
O II				
834.47	8.61e+00	2 - 4	0.00 - 119837.21	$2s^2 2p^3 - 2s 2p^4$
833.33	8.65e+00	4 - 6	0.00 - 120000.43	$2s^2 2p^3 - 2s 2p^4$
832.76	8.67e+00	4 - 2	0.00 - 120082.86	$2s^2 2p^3 - 2s 2p^4$
539.85	9.81e+00	4 - 2	0.00 - 185235.281	$2s^2 2p^3 - 2s^2 2p^2 3s$
539.55	9.81e+00	4 - 4	0.00 - 185340.577	$2s^2 2p^3 - 2s^2 2p^2 3s$
539.09	9.83e+00	4 - 6	0.00 - 185499.124	$2s^2 2p^3 - 2s^2 2p^2 3s$
538.26	5.18e+01	6 - 4	26810.55 - 212593.82	$2s^2 2p^3 - 2s 2p^4$
537.83	5.73e+01	4 - 2	26830.57 - 212762.25	$2s^2 2p^3 - 2s 2p^4$
430.18	4.36e+01	4 - 6	0.00 - 232462.724	$2s^2 2p^3 - 2s^2 2p^2 3d$
430.04	4.13e+01	4 - 4	0.00 - 232535.949	$2s^2 2p^3 - 2s^2 2p^2 3d$
429.92	4.25e+01	4 - 2	0.00 - 232602.492	$2s^2 2p^3 - 2s^2 2p^2 3d$
O III				
835.29	5.99e+00	5 - 7	306.174 - 120025.2	$2s^2 2p^2 - 2s 2p^3$
835.09	1.44e+00	5 - 5	306.174 - 120053.4	$2s^2 2p^2 - 2s 2p^3$
833.75	4.58e+00	3 - 5	113.178 - 120053.4	$2s^2 2p^2 - 2s 2p^3$
833.72	2.48e+00	3 - 3	113.178 - 120058.2	$2s^2 2p^2 - 2s 2p^3$
832.93	3.41e+00	1 - 3	0.00 - 120058.2	$2s^2 2p^2 - 2s 2p^3$
703.85	1.37e+01	5 - 5	306.174 - 142381.0	$2s^2 2p^2 - 2s 2p^3$
703.85	7.54e+00	5 - 3	306.174 - 142381.8	$2s^2 2p^2 - 2s 2p^3$
702.90	4.47e+00	3 - 5	113.178 - 142381.0	$2s^2 2p^2 - 2s 2p^3$
702.90	4.66e+00	3 - 3	113.178 - 142381.8	$2s^2 2p^2 - 2s 2p^3$
702.84	1.83e+01	3 - 1	113.178 - 142393.5	$2s^2 2p^2 - 2s 2p^3$
702.34	6.06e+00	1 - 3	0.00 - 142381.8	$2s^2 2p^2 - 2s 2p^3$
508.18	8.04e+01	5 - 3	306.174 -197087.7	$2s^2 2p^2 - 2s 2p^3$
507.68	4.82e+01	3 - 3	113.178 - 197087.7	$2s^2 2p^2 - 2s 2p^3$
507.39	1.61e+01	1 - 3	0.00 - 197087.7	$2s^2 2p^2 - 2s 2p^3$
373.80	9.50e+00	3 - 5	113.178 - 267634.0	$2s^2 2p^2 - 2s^2 2p 3s$
374.00	1.26e+01	1 - 3	0.00 - 267377.1	$2s^2 2p^2 - 2s^2 2p 3s$
374.07	2.85e+01	5 - 5	306.174 - 267634.0	$2s^2 2p^2 - 2s^2 2p 3s$
374.16	9.46e+00	3 - 3	113.178 - 267377.1	$2s^2 2p^2 - 2s^2 2p 3s$
374.33	3.79e+01	3 - 1	113.178 - 267258.7	$2s^2 2p^2 - 2s^2 2p 3s$
374.43	1.58e+01	5 - 3	306.174 - 267377.1	$2s^2 2p^2 - 2s^2 2p 3s$

Wavelength, A	$A_{ik}, 10^8 s^{-1}$	g_i - g_k	E_i - E_k, cm^{-1}	Configurations
O IV				
1343.51	2.57e+00	4 - 6	180724.2 - 255155.9	$2s2p^2 - 2p^3$
1342.99	4.29e-01	4 - 4	180724.2 - 255184.9	$2s2p^2 - 2p^3$
1338.62	2.17e+00	2 - 4	180480.8 - 255184.9	$2s2p^2 - 2p^3$
923.44	4.39e+00	4 - 2	180724.2 - 289015.4	$2s2p^2 - 2p^3$
923.37	1.10e+01	4 - 4	180724.2 - 289023.5	$2s2p^2 - 2p^3$
921.37	8.83e+00	2 - 2	180480.8 - 289015.4	$2s2p^2 - 2p^3$
921.30	2.21e+00	2 - 4	180480.8 - 289023.5	$2s2p^2 - 2p^3$
802.25	4.05e+00	2 - 2	164366.4 - 289015.4	$2s2p^2 - 2p^3$
802.20	4.05e+00	2 - 4	164366.4 - 289023.5	$2s2p^2 - 2p^3$
790.20	7.08e+00	4 - 6	385.9 - 126936.3	$2s^22p - 2s2p^2$
790.11	1.18e+00	4 - 4	385.9 - 126950.2	$2s^22p - 2s2p^2$
787.71	5.95e+00	2 - 4	0.00 - 126950.2	$2s^22p - 2s2p^2$
780.00	9.70e-01	4 - 6	126950.2 - 255155.9	$2s2p^2 - 2p^3$
779.91	1.36e+00	6 - 6	126936.3 - 255155.9	$2s2p^2 - 2p^3$
779.82	1.31e+00	4 - 4	126950.2 - 255184.9	$2s2p^2 - 2p^3$
779.74	1.46e+00	6 - 4	126936.3 - 255184.9	$2s2p^2 - 2p^3$
617.03	2.89e+01	4 - 2	126950.2 - 289015.4	$2s2p^2 - 2p^3$
617.01	2.89e+00	4 - 4	126950.2 - 289023.5	$2s2p^2 - 2p^3$
616.95	2.60e+01	6 - 4	126936.3 - 289023.5	$2s2p^2 - 2p^3$
609.83	2.40e+01	4 - 2	385.9 - 164366.4	$2s^22p - 2s2p^2$
608.40	1.21e+01	2 - 2	0.00 - 164366.4	$2s^22p - 2s2p^2$
555.27	2.41e+01	4 - 2	385.9 - 180480.8	$2s^22p - 2s2p^2$
554.51	6.06e+01	4 - 4	385.9 - 180724.2	$2s^22p - 2s2p^2$
554.01	4.86e+01	2 - 2	0.00 - 180480.8	$2s^22p - 2s2p^2$
553.33	1.22e+01	2 - 4	0.00 - 180724.2	$2s^22p - 2s2p^2$
O V				
1371.30	3.34e+00	3 - 5	158797.7 - 231721.4	$2s2p - 2p^2$
774.52	3.80e+01	3 - 1	158797.7 - 287910.3	$2s2p - 2p^2$
629.73	2.87e+01	1 - 3	0.00 - 158797.7	$2s^2 - 2s2p$
248.46	5.59e+01	3 - 1	158797.7 - 561276.4	$2s2p - 2p3s$
O VI				
1037.61	4.16e+00	2 - 2	0.00 - 96375.0	$1s^22s - 1s^22p$
1031.91	4.09e+00	2 - 4	0.00 - 96907.5	$1s^22s - 1s^22p$
184.117	1.14e+02	4 - 2	96907.5 - 640039.	$1s^22p - 1s^23s$
183.937	5.70e+01	2 - 2	96375.0 - 640039.	$1s^22p - 1s^23s$

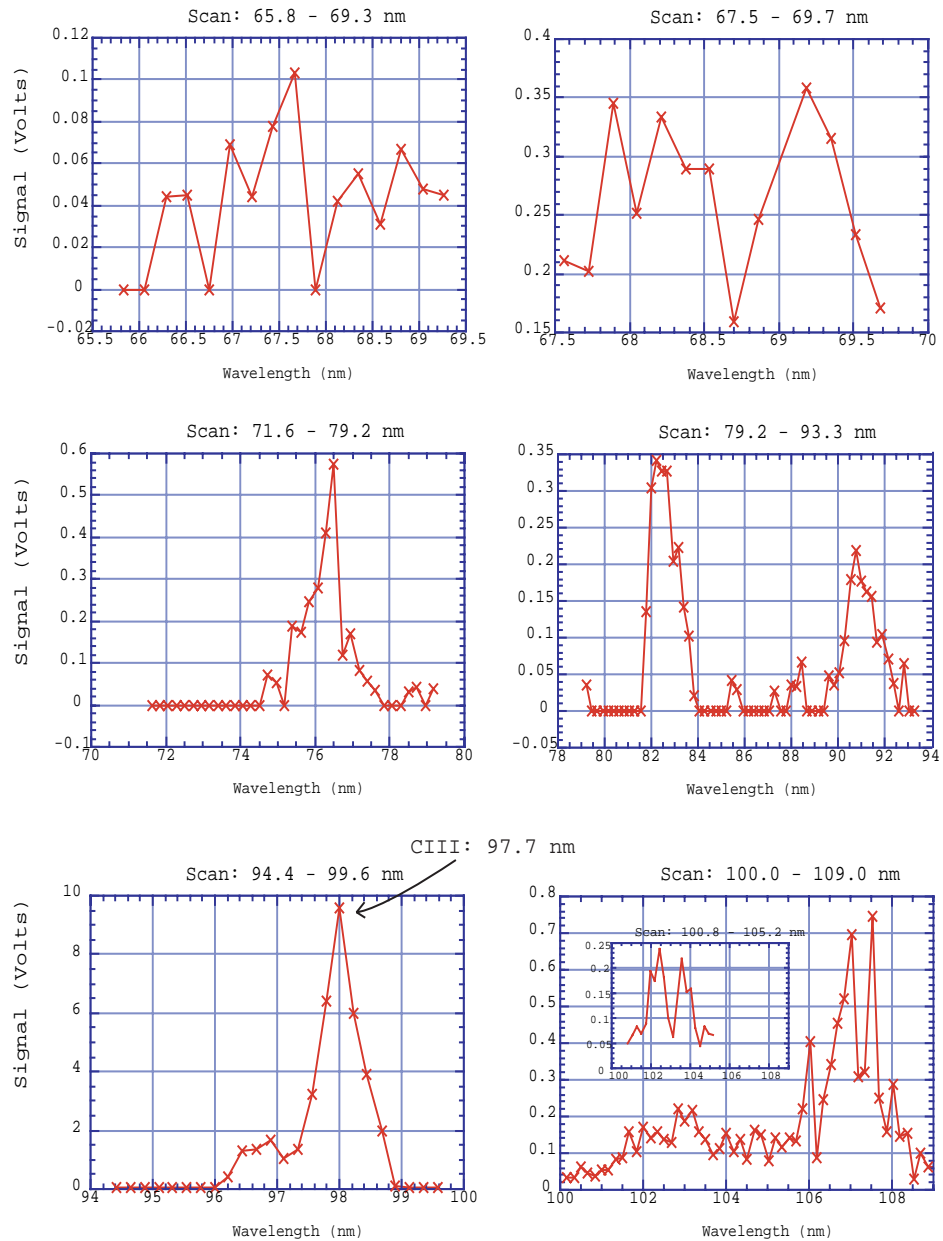# B. VUV Monochromator Wavelength Calibration Scans

Figure 21: A) The VUV monochromator wavelength calibration scans covering most of the region between about 65 nm and 108 nm.
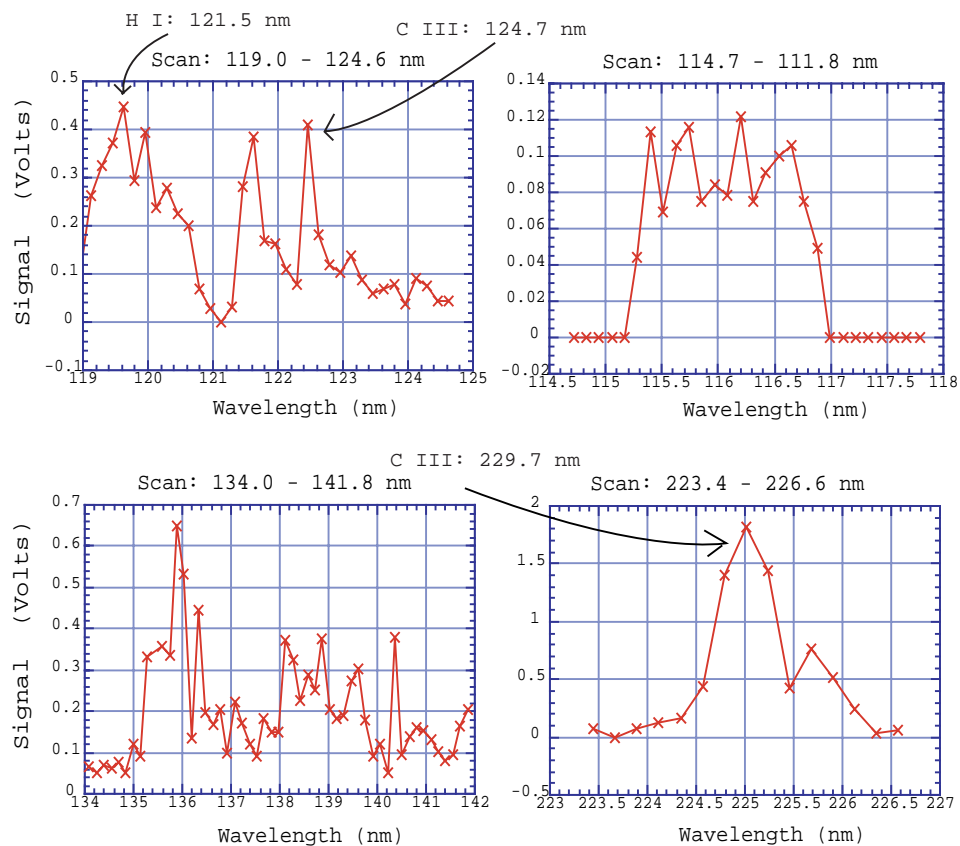
Figure 21: B) The VUV monochromator wavelength calibration scans in several regions above 115 nm.

Note, the magnitudes of the peaks in the figures presented below should not be compared between different figures, as conditions under which the data was taken were varied.

C. Summary of Ionization/Recombination and Excitation/De-excitation Rates Used in the Impurity Emission Code

Here, we follow the presentation of the material by I. H. Hutchinson.[13]

Radiative transitions

We first consider the simplest case of radiative transitions. Let i and j denote two excitation levels of a particular ion. And let E_i and E_j ($E_i > E_j$) be their corresponding energies. Then, an atom with an electron on the ith level can spontaneously decay to the lower lying j^{th} level with the emission of a photon of frequency ν_{ij}:

$$h\nu_{ij} = E_i - E_j \tag{48}$$

The probability per unit time of such spontaneous de-excitation is usually denoted by A_{ij}. There are two other radiative transition probabilities associated with the ith and j^{th} energy levels. An ion on the jth excitation level can absorb a photon and be excited to the ith excitation level with the probability per unit time of $B_{ji}\rho(\nu_{ij})$, where $\rho(\nu)$ is the density per unit frequency of electromagnetic radiation at the atom (or simply density of photons with energy $h\nu_{ij}$). Or, an induced decay form the ith to the jth energy level can occur due to the presence of radiation with the probability per unit time of $B_{ij}\rho(\nu_{ij})$

Now, consider a collection of ions in complete thermal equilibrium at temperature T with N_i ions on the ith excitation level and N_j ions on the jth excitation level. Since the system is in thermal equilibrium,

$$\frac{N_i}{N_j} = \frac{g_i}{g_j} e^{-\frac{E_i - E_j}{T}} = \frac{g_i}{g_j} e^{-\frac{h\nu_{ij}}{T}}, \tag{49}$$

where g_k is the number of degenerate quantum states of the kth energy level; and

$$\rho(\nu) = \frac{8\pi h\nu^3}{c^3} \left[e^{h\nu/T} - 1 \right]^{-1}, \tag{50}$$

is the blackbody level of radiation at temperature T.

Since the system is at equilibrium, the number of transitions from the ith to the jth energy level should be equal to the number of transitions in the opposite direction. That condition is called 'the principle of detailed balance', and we have

$$(A_{ij} + B_{ij}\rho)N_i = B_{ji}\rho N_j \tag{51}$$

Then, from Eq. 49, Eq. 50 and Eq. 51 it follows that

$$A_{ij} = \frac{8\pi h\nu_{ij}^3}{c^3} B_{ij}. \tag{52}$$

The probability of absorption B_{ij} is, in turn, proportional to the, so called, line strength S_{ij} of the $i - j$ transition:

$$S_{ij} = \sum_{m_i, m_j} |\langle i, m_i | e\hat{\mathbf{r}} | j, m_j \rangle|^2, \tag{53}$$

which is just a sum over all degenerate states of the square magnitude of the corresponding matrix elements of the atomic dipole moment. Therefore, in order to know the value of A_{ij}, one only needs to determine the wavefunctions of these quantum states. However, these are known exactly only for one-electron atoms[2], while for atoms with more than one electron application of various quantum mechanical approximation methods is required.[12][11]

Collisional transitions

The determination of cross-sections and rate coefficients for atomic collisional processes forms a subfield of physics in and of itself. Even the best known theoretical calculations of the collisional rate coefficients are subject to uncertainties that be as great as a factor of two.[13] Therefore, here, I will not attempt any theoretical arguments and will limit myself to basic diagrams of the considered physical processes, together with the estimated rate coefficients used in the impurity emission code.

In the equations below, Z is the atomic number, T is the temperature, χ_i is the ionization potential of the ith ion of a given atom, $R_y = 1.0974 \times 10^7 \ (m^{-1})$ is the Rydberg constant, n_0 is the principal quantum number of the lowest incomplete shell of the ion. The electron velocity distribution is assumed to be the Maxwellian distribution.
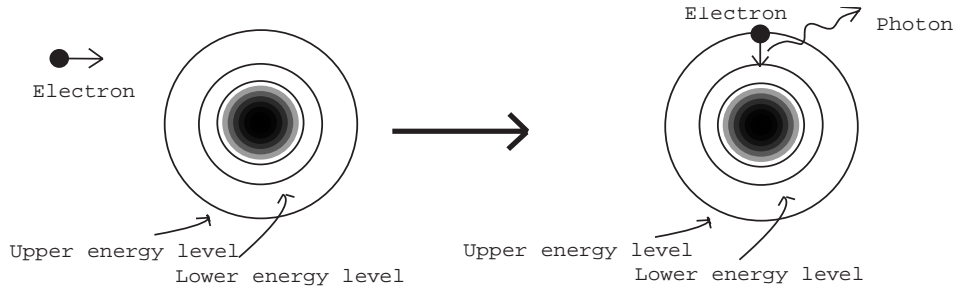
- Radiative Recombination:

Figure 22: Schematic representation of radiative recombination of an ion, where electron is captured by the ion into some high bound state. The capture is followed by a spontaneous radiative transition downward.

$$\langle \sigma_{rr} v \rangle_i \approx 5.2 \times 10^{-20} \frac{Z}{2} \left(\frac{Z^2 R_y}{T} \right)^{1/2}$$
$$\times \left[1 - exp\left\{ \frac{-\chi_i}{T} \left[1 + \frac{1}{n_0} \left(\frac{\xi}{n_0^2} - 1 \right) \right] \right\} \right] \left[(ln \tfrac{\chi_i}{T})^2 + 2 \right]^{1/2} \ (m^3 s^{-1}) \tag{54}$$
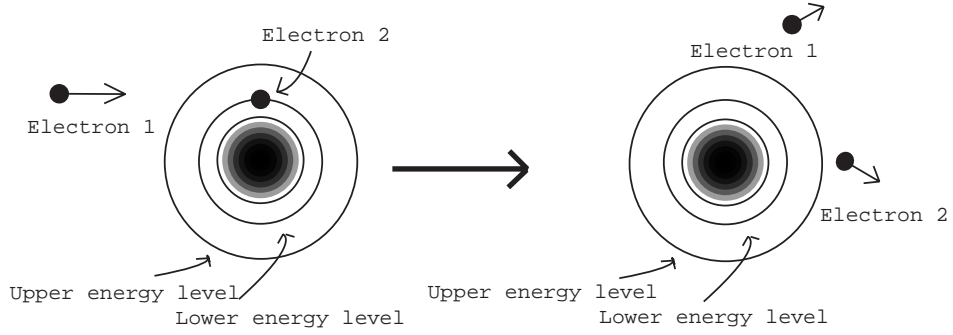
- Collisional Ionization:

Figure 23: Schematic representation of collisional ionization of an atom, where 'Electron 1' "knocks off" 'Electron 2' from the atom and is, in turn, scattered itself.

$$\langle \sigma_{ci} v \rangle_i = g(1.7 \times 10^{-14}) \left[\frac{R_y}{\chi_i} \right]^2 \left[\frac{T}{R_y} \right]^{1/2} e^{\frac{-\chi_i}{T}} \left[1 - e^{\frac{-5\chi_i}{T}} \right] (m^3 s^{-1}), \qquad (55)$$

where the Gaunt factor g is

$$g = 1 + \frac{\sqrt{3}}{\pi} ln\left(1 + \frac{T}{\chi_i} \right). \qquad (56)$$

- Collisional Excitation:
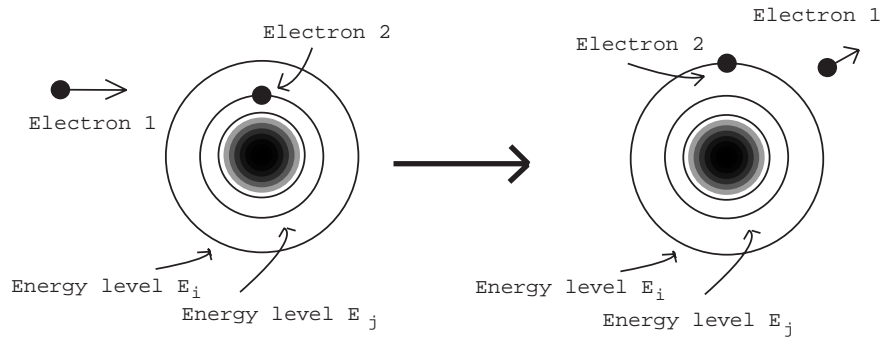
Figure 24: Schematic representation of collisional excitation of an atom, where 'Electron 1' is scattered by the atom and an energy transfer between the electron and the atom takes place, so that 'Electron 2' is excited from the jth to the ith energy level.

$$\langle\sigma_{ce}v\rangle_{ij} = g(3.15\times10^{-13})f_{ji}\frac{R_y}{E_{ij}}\left(\frac{R_y}{T}\right)^{1/2}e^{\frac{-E_{ij}}{T}}\ (m^3s^{-1}), \tag{57}$$

where the Gaunt factor g is

$$g \approx 0.2 + \frac{\sqrt{3}}{\pi}ln\left(1+\frac{T}{E_{ij}}\right). \tag{58}$$
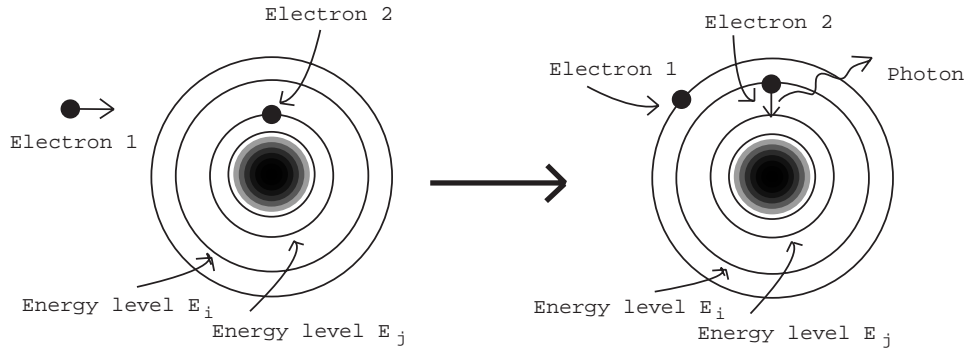
- Dielectronic Recombination:

Figure 25: Schematic representation of dielectronic recombination of an atom, where the capture of 'Electron 1' happens simultaneously with the excitation of 'Electron 2' from the jth to the ith energy level, which is followed by a radiative transition of 'Electron 2' back to the jth energy level.

$$\langle\sigma_{der}v\rangle_{ij} = (8.8\times10^{-18})f_{ji}Z^{2/3}\frac{E_{ij}}{R_y}\left(\frac{R_y}{T}\right)^{3/2}e^{\frac{-E_{ij}}{T}}\ (m^3s^{-1}). \tag{59}$$

D. The Simplex Algorithm and Its Application to the Problem of Time Dependent Parameter Fitting

Simplex Algorithm

The simplex algorithm described in 'Numerical recipes" by W.H. Press, *et al*[24] is an algorithm to find a local minimum of a multivariable single-valued function. So that given $f: \mathbf{R}^n \rightarrow \mathbf{R}$, the algorithm outputs a vector $\mathbf{v} \in \mathbf{R}^n$ s.t. $f(\mathbf{v})$ is a local minimum.

The basic idea of the simplex algorithm is to start with (n+1) vectors forming an n-tetrahedron in the n-dimensional space and move its vertices "downhill" until the relative difference between the values of f at the best vertex v_{best} ($f(v_{best})$has the lowest value) and at the worst vertex v_{worst} ($f(v_{worst})$has the highest value) is less than a certain predetermined tolerance value. The 'moves' allowed by the algorithm are:

reflection reflecting v_{worst} across the opposite face of the tetrahedron;

extended reflection same as reflection, but considers a point further away from the reflecting face;

injection replaces v_{worst} with a point inside the tetrahedron;

contraction contraction of the tetrahedron around v_{best}.

Running the algorithm several times might be necessary if one wants to find the absolute minimum of f.

A potential problem arises when one considers the tolerance function. Taking simple relative difference [4] is clearly not sufficient when $f = 0$ at a local minimum. Some other tolerance function should be applied in a case like that.

Simplex Algorithm in Data Fitting

Suppose one has a set of data $S = \{s_n\}$ collected over time. (For example, the number of particles detected over a given interval of time with time step *dt*). Furthermore, suppose that a function *g(t; a(t), b(t))* describes the physical laws governing the processes which generate the data (for example, the rate of decay), where the dependence of the parameters *a(t)* and *b(t)* on time is unknown.

We can use the simplex algorithm to determine *a(t)*, *b(t)* and thus *g(t)*. Define f, as above, to be $f_n(a_n, b_n) = |g((n * dt); a_n, b_n) - s_n|$ for the nth time step. Applying the simplex algorithm to each consecutive f_n to find the values of a_n and b_n for which f_n is zero, we find the time profiles for *a(t)* and *b(t)*.

Note that here we are faced with the exact problem described in the previous section. Namely, $f_n = 0$ is the absolute minimum condition on f_n.

---

[4]$2*(f(v_{worst})-f(v_{best})) / (f(v_{worst})+f(v_{best}))$

Determining the Time Profiles of Plasma Temperature and Density from Impurity Emission Data

As described in the Section 2.3 of this thesis, the intensity of a given emission line of a certain ionization state of a certain atom has functional dependence on the plasma temperature T_e, plasma density n_e, and the population of that ionization state (which itself depends on T_e and n_e). Then, using collected data of line intensity from several emission lines, one should be able to determine the approximate time profiles of electron temperature and density, as described above.

One of the important algorithmic problems one notices very soon, is that T_e and n_e are both naturally restricted to the first quarter of the $T_e \times n_e$ parameter space. As the original simplex algorithm does not account for such restrictions, some modifications have to be made. In the current working algorithm, a simple reflection of any vertices attempting to escape the first quarter back into the first quarter suffices.

The modified simplex algorithm is implemented in Matlab in routine "mysimplex.m".

E. Acknowledgments

References

[1] J. J. Ambrosiano, W. H. Matthaeus, M. L. Goldstein, D. Plante (1988), *Journal of Geophysical Research*, No 93, p. 14383.

[2] H. A. Bethe, E. E. Salpeter (1957), **Quantum Mechanics of One- and Two-Electron Systems** (Academic Press).

[3] M. R. Brown (1999), *Physics of Plasmas*, Vol 6, No 5, p. 1717.

[4] L. F. Burlaga (1995), **Interplanetary Magnetohydrodynamics** (Oxford University Press).

[5] F. F. Chen (1974), **Introduction to Plasma Physics** (Plenum Press).

[6] P. G. Carolan and V. A. Piotrowicz (1983), *Plasma Physics*, Vol 25, No 10, pp. 1065 - 1086.

[7] C. G. R. Geddes, T. W. Kornack, M. R. Brown (1998), *Physics of Plasmas*, No 5, p. 1027.

[8] M. L. Goldstein, W. H. Matthaeus, J. J. Ambrosiano (1986), *Geophysical Research Letters*, Vol 13, No 3, p. 205.

[9] R. J. Goldston, P. H. Rutherford (1995), **Introduction to Plasma Physics** (Institute of Physics Publishing).

[10] P. Gray, W. H. Matthaeus (1992), **Particle Acceleration in Cosmic Plasmas: MHD Turbulence, Reconnection, and Test-Particle Acceleration**, edited by G. P. Zank and T. K. Gaisser (AIP Press).

[11] H. R. Griem (1964), **Plasma Spectroscopy** (McGraw-Hill Book Company).

[12] D. G. Hartree (1957), **The Calculation of Atomic Structure** (John Wiley & Sons, Inc).

[13] I. H. Hutchinson, **Principles of Plasma Diagnostics** (Cambridge University Press).

[14] T. W. Kornack, P. K. Sollins, M. R. Brown (1998), *Physical Review E*, Vol 58, No 1, p. 36.

[15] T. W. Kornack, (1998), **Magnetic Reconnection Studies on SSX** (Undergraduate thesis, Swarthmore College)

[16] R. H. Landau, M. J. Paez Mejia (1997), **Computational Physics: Problem Solving with Computers**, (John Wiley & Sons, Inc).

[17] W. Lochte-Holtgreven (1995), **Plasma Diagnostics**, (AIP Press).

[18] S. L. Mandelshtam and N. J. Suhariev (1953), *Zhurnal eksperimentalnoy i teoreticheskoy Fiziki*, No 24, p. 701.

[19] W. H. Matthaeus, J. J. Ambrosiano, M. L. Goldstein (1984), *Physical review Letters*, Vol 53, No 15, p. 1449.

[20] R. W. P. McWhirter (1965), **Plasma Diagnostic Techniques**, (Academic Press).

[21] R. L. Morse (1991), **Encyclopedia of Physics: Plasmas**, edited by R. G. Lerner and G. L. Trigg (VCH Publishers).

[22] E. Parker (1963), *Journal of Geophysical Research*, No 62, p. 509.

[23] I. M. Podgornyi (1971), **Topics in Plasma Diagnostics**, (Premium Press).

[24] W. H. Press, B. P. Flannery, S. A. Teukolsky, W. T. Vetterling (1986), **Numerical Recipes: The Art of Scientific Computing**, (Cambridge University Press).

[25] J. A. R. Samson, **Techniques of Vacuum Ultraviolet Spectroscopy**, (Pied Publications).

[26] D. D. Schnack, I. Lottati, Z. Mikic, P. Satyanarayana (1998), *Journal of Computational Physics*, No 140, pp. 71-121.

[27] L. Spitzer (1956), **Physics of Fully Ionized Gases**, (Interscience).

[28] S. Suckewer (1968), *Plasma Physics*, Vol 10, pp. 527-542.

[29] S. Suckewer (1967), *Physics Letters*, Vol 25A, No 3, pp. 284-285.

[30] S. Suckewer (1967), *Physics Letters*, Vol 25A, No 5, pp. 405-406.